75dBm EIRP W-band Electronic 2-D Beam-steering Antenna Integrated with a GaAs Array Transmitter via Quasi-Optical Spatial Power

Citation for the original published paper (version of record):
Chernikov, V., Vilenskiy, A., Granström, G. et al (2026). 75dBm EIRP W-band Electronic 2-D Beam-steering Antenna Integrated with a GaAs Array Transmitter via Quasi-Optical Spatial Power Combining. IEEE Transactions on Antennas and Propagation, 74(6): 5223-5238. http://dx.doi.org/10.1109/TAP.2026.3675742

A 75-dBm EIRP W-Band Electronic 2-D Beam-Steering Antenna Integrated With a GaAs Array Transmitter via Quasioptical Spatial Power Combining

Viktor S. Chernikov, *Graduate Student Member, IEEE*, Artem R. Vilenskiy, *Senior Member, IEEE*, Göran Granström, Lars Manholm, Sam Agneessens, *Member, IEEE*, Marcus Gavell, *Member, IEEE*, and Marianna V. Ivashina, *Senior Member, IEEE*

***Abstract*—We present a W-band (92–96 GHz) electronically steerable reflector antenna system for 6G backhaul that co-integrates a GaAs multichannel transmitter (Tx) with a compact waveguide (WG) focal-plane array (FPA) via a quasioptical feeding network (QOFN). Unlike conventional architectures that separate power amplifier (PA) power combining and beamforming into distinct modules, or switch a single PA among QOFN inputs, the proposed QOFN simultaneously combines the power of all PAs while synthesizing the required FPA excitation for electronic beam steering. This eliminates a separate lossy switch/combiner stage and equalizes per-channel power, critical for maintaining high Tx efficiency. Methodologically, we develop an active-system modeling framework that extends conventional passive antenna array formulations by incorporating PA output mismatch effects, channel-to-channel variations, and discrete phase-shifter states into the beam synthesis. The formulation yields closed-form realized gain and effective isotropic radiated power (EIRP) maximization solutions under realistic PA constraints. To compensate for mast swaying, a rim-extended offset parabolic reflector is co-designed with the FPA, providing ~50-dBi gain with ETSI Class 3 sidelobe mask compliance over a 2-half-power-beamwidth 2-D steering range. A prototype with six Tx PAs shows that across 92–96 GHz and multiple beams, the minimum measured EIRP is ≥ 75 dBm, the on-axis beam reaches ~80 dBm, and the QOFN insertion loss is 2.3–3.7 dB. The results experimentally validate a unified architectural and modeling approach to high-EIRP W-band backhaul TXs, demonstrating a compact and scalable alternative to large silicon-based phased arrays that typically peak near 60-dBm EIRP.**

***Index Terms*—6G, active antenna, beamforming network, millimeter-wave, phased array, transmitting antenna.**

Received 14 November 2025; revised 24 February 2026; accepted 7 March 2026. Date of publication 27 March 2026; date of current version 11 June 2026. This work was supported by the “ENERGETIC” Project through VINNOVA under Grant 2021-01337 and in part by Sweden-Taiwan Collaborative Project “Antennas Beyond 5G” by the Swedish Foundation for Strategic Research Stiftelsen för Strategisk Forskning (SSF). *(Corresponding author: Viktor S. Chernikov.)*

Viktor S. Chernikov and Mariannna V. Ivashina are with the Antenna Systems Group, Department of Electrical Engineering, Chalmers University of Technology, 41296 Gothenburg, Sweden (e-mail: viktorch@chalmers.se; marianna.ivashina@chalmers.se).

Artem R. Vilenskiy was with the Antenna Systems Group, Department of Electrical Engineering, Chalmers University of Technology, 41296 Gothenburg, Sweden. He is now with XPANCEO Research on Natural Science, Dubai, United Arab Emirates (e-mail: artem.vilenskiy@chalmers.se).

Göran Granström and Marcus Gavell are with Gotmic AB, 41133 Gothenburg, Sweden (e-mail: goran.granstrom@gotmic.se; marcus.gavell@gotmic.se).

Lars Manholm and Sam Agneessens are with Ericsson Research, Ericsson, 41756 Gothenburg, Sweden (e-mail: lars.manholm@ericsson.com; sam.agneessens@ericsson.com).

Digital Object Identifier 10.1109/TAP.2026.3675742

I. Introduction

THE rollout of next-generation wireless systems, 6G, is expected to demand higher capacity and flexible deployment, especially for high-data-rate point-to-point (P2P) backhaul links. To meet these needs, activity is moving into the underutilized E-, W-, and D-bands (60–170 GHz), which offer abundant spectrum for multi-Gb/s links [1]. Commercial E-band (71–86 GHz) systems already deliver up to 25 Gb/s over 1–3 km [2]. In contrast, W-/D-band demonstrations have reached 100 Gb/s over subkilometer distances, but wide deployment has not yet followed.

Operation at the W-/D-band entails severe free-space path loss—over 130 dB at 90 GHz (W-band) for 1 km versus ~120 dB at 5G millimeter-wave bands. To compensate for this loss, it is essential to achieve a high effective isotropic radiated power (EIRP) that requires a combination of high TX output power and high-gain antennas. Recent W-band trials with 30–34-dBi antennas report saturated EIRP of 52–60 dBm and demonstrated over a few hundred meters to 1-km links. However, reaching EIRP beyond 60 dBm, as required for longer links [3], demands either higher transmit power or greater antenna gain, or both, tightening requirements on millimeter-wave power generation, beam pointing, and regulatory limits (e.g., sidelobe masks and transmit power).

Accurate beam pointing is challenging with ultrahigh-gain apertures. For example, a 50-dBi-gain antenna has a half-power beamwidth (HPBW) of 0.5° [4]. Such narrow beams are sensitive to misalignment, requiring mechanical or electronic beamsteering over several HPBWs in 2-D [5], [6], [7]. In scenarios such as addressed in this work, where the required beamsteering range is moderate compared to typical millimeter-wave phased arrays [8], [9], [10], [11], [12], solutions based on large reflectors or lens antennas with small-scale array feeds are most practical [13], [14], [15], [16], [17], [18], [19]. However, these systems have competing design constraints, that is, the array element aperture increases to shape reflector/lens illumination, versus minimizing interelement spacing to form closely overlapping steered beams.

Efficient generation of TX output power is fundamentally constrained by limitations in semiconductor technologies and integrated circuit (IC) design. In the aforementioned backhaul systems, power amplifier (PA) ICs provide only low-to-moderate output levels (2–10 dBm), even at the E-band. Analysis of mature silicon-based technologies at the W-band, such as CMOS and SiGe BiCMOS [20], shows that PAs typically achieve saturated output power (P_{sat}) up to 20 dBm, with the maximum power-added efficiency (PAE) of 17% [21], [22], [23]. The III–V compound semiconductor technologies, including GaN and (Al)GaAs, improve performance, with P_{sat} values reaching 27–30 dBm and PAE of about 10% for GaAs and 15% for GaN [24], [25], [26]. Nevertheless, these technologies have limited commercial availability, low fabrication yield, and higher cost, particularly for GaN.

Consequently, power combining from multiple PAs is required to scale up P_{sat}. Conventional methods, based on on-chip combiners [27], [28] or off-chip integrated passive combining networks [29], [30], [31], introduce losses that grow with frequency and the number of PAs. On-chip combiners are affected by high insertion losses of the corporate combining networks, while off-chip solutions are typically single-output designs, which require the use of a switching network after them to comply with focal plane array (FPA) operation.

An alternative is on-antenna power combining [32], [33], [34], [35], [36], where multiple PAs directly feed a single element (e.g., a patch, or slot) via multiport excitation, while matching the antenna ports to the optimal (non-50Ω) load impedances of the PAs. This enables more efficient power combining, but requires antenna-PA co-design, which is especially challenging at high frequencies. Most demonstrations to date have focused on boosting P_{sat} and efficiency, while minimizing degradation of the antenna pattern due to nonlinear effects. This approach applies to conventional phased-array systems where all array elements equally contribute to the radiation field during beam steering, in contrast with the FPA-fed reflector systems requiring effective excitation of only a part of an FPA aperture. In contrast, key objectives of active arrays, such as advanced beamforming and beamsteering, remain unexplored at millimeter-wave frequencies.

The prevalent approach of treating array beamforming and PA power combining as functionalities realized in separate modules in TX front-end design has been studied in [37], along with the potential of joint power combining and beamforming [38] for high-EIRP systems. The latter introduced the concept of unified spatial power combining and beam steering using multiple-input–multiple-output quasioptical feeding networks (QOFNs) [39]. However, these prior studies focused primarily on passive or conceptual network-level implementations and did not demonstrate an integrated front end operating under practical constraints, such as impedance mismatch, finite phase resolution, and nonidentical active channels (ACs). Several conventional beamforming networks can be adopted for this scenario. For example, the Butler matrix [40], [41] can combine the power of phased output (“antenna”) ports into the input (“beam”) ports, when operated in reverse. However, its corporate implementation introduces insertion loss that scales with frequency and channel count, and it requires equality between the number of input N and output M ports ($N = M$), limiting scalability for high-power applications. Rotman-lens and related QOFNs [42], [43] remove the strict $N = M$ constraint, yet they are typically optimized for beam switching rather than efficient multi-PA power combining.

In contrast to these prior approaches, this work advances the QOFN concept from a passive beamforming structure to a fully integrated active front end. Building on in [38], we present a novel W-band reflector antenna system in which a multichannel GaAs TX and a compact waveguide (WG) FPA are co-integrated through a dedicated multiple-input QOFN that performs joint spatial power combining and electronic beam steering within a single component. The main contributions of this work are as follows.

1) An integrated high-EIRP front-end architecture that enables simultaneous spatial power combining and electronic beam steering using a multiple-input QOFN, directly addressing the W-/D-band design challenges associated with limited PA output power and high insertion loss of postamplifier combining or switching networks [44].
2) An active-system quasioptical beamforming formulation based on embedded-element patterns (EEPs) referenced to the TX input, linking PA reflection coefficients, channel-to-channel variations, and quantized phase control to the beamformed array pattern and EIRP. This extends conventional embedded-element superposition approaches to an active TX–antenna system model and yields closed-form solutions for realized gain and EIRP maximization under per-channel power constraints.
3) A reflector-FPA co-design strategy employing a rim-extended offset parabolic reflector optimized together with FPA to achieve near-50-dBi gain with ETSI Class 3 sidelobe-mask compliance over a 1° 2-D range.[1]
4) Experimental validation at the W-band through a six-channel GaAs prototype demonstrating ≥ 75-dBm measured EIRP across multiple beams.

Thus, the novelty of the present work lies not merely in subsystem integration but in the unified architectural and analytical treatment of spatial power combining and beam steering in a reflector-based W-band TX front end, supported by experimental validation at high EIRP.

The article is organized as follows. Section II describes the system and its generalized model. Sections III and IV develop the beamforming framework for the passive antenna system and complete active front end, respectively. Section V describes the design implementation. Sections VI and VII report the passive and active system results, respectively. Section VIII discusses tradeoffs and comparison with the state of the art. Section IX concludes the work and outlines directions for future research.

II. System Model and Methodology

A high EIRP of the antenna system is primarily achieved through the design of an integrated front-end architecture that enables simultaneous spatial power combining and electronic beamsteering using a multiple-input QOFN. To formalize this

[1]In this work, the ETSI E-band mask is adopted as the closest available regulatory benchmark defined for fixed P2P links.

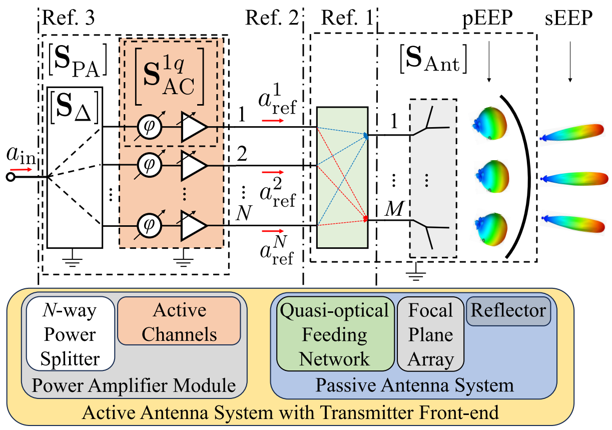

Fig. 1. Generalized representation of the proposed W-band active TX front end employing a quasioptical feeding network (QOFN) that enables joint power combining and beamforming/beamsteering. The system comprises N ACs in the PA module and an M-element FPA feeding a reflector. Reference planes: 1) QOFN outputs toward FPA; 2) QOFN inputs from PA module; and 3) splitter input.

architecture and describe the design procedure of the entire active antenna system, we utilize the generalized system representation as shown in Fig. 1 for the N ACs of the PA module and the M-elements of the FPA feeding a reflector antenna, which are interconnected through the $N \times M$ quasioptical feeding network (QOFN).

This representation defines two main parts of the system: 1) the PA module and 2) the passive antenna system—both include multiple components. Each component is characterized by scattering matrices, large-signal responses (PA module), and, for the passive antenna, by EEPs. All S-parameters are de-embedded to the stated reference planes. In the small-signal regime, this representation turns end-to-end performance evaluation into a linear microwave-circuit problem, along with a radiation problem with compact quadratic figures of merit. The proposed approach resembles the established modeling framework for active beamforming array systems (see [17], [45]), adapted here to the antenna–TX case with joint power combining and beamforming.

A PA Module (Ref. 3 → Ref. 2)

The N-way WG splitter (Ref. 3) provides a uniform RF power distribution to the N ACs; its S-parameters are $\mathbf{S}_{\Delta}$. Each AC comprises a phase shifter (PS) and a PA chain, creating the capability of tuning the phase and magnitude of its transmission coefficient, while the final amplification stage provides the required output power level. We index the AC state by q, defining the discretized phase and amplitude range of the PA chain; the pth channel state is described by $\mathbf{S}_{\mathrm{AC}}^{(p,q)}$. Each PA chain comprises a driver PA (DPA) and a high-power PA (HPA; see details on the PA architecture in Section V-C). AC-to-AC spread is accounted for by the per-channel P_{sat} (and optionally $P_{1\mathrm{dB}}$) defined by the HPA. The input/output impedance match effects of the ACs are included via their reflection coefficients at Ref. 2 and Ref. 3. A detailed PA module design is provided in Section V-C.

B Passive Antenna System (Ref. 2 → EEPs)

The QOFN is realized as a parallel-plate WG (PPWG) region with N input and M output ports (see the details of the design in Section VI-A). Together with the FPA and reflector, it forms the passive antenna system. We use $\mathbf{S}_{\mathrm{FPA+QOFN}}$ for the FPA + QOFN block and $\mathbf{S}_{\mathrm{Ant}}$ for the complete passive antenna system, including the reflector. For the offset parabolic reflector used here (Section V-A), we expect a negligible change in port behavior at Ref. 2, since the central blockage effect is mitigated by the sufficient clearance distance. Hence, we set $\mathbf{S}_{\mathrm{FPA+QOFN}} \approx \mathbf{S}_{\mathrm{Ant}}$. To analyze radiation performance, we define primary EEPs (pEEPs) for the FPA + QOFN part and secondary EEPs (sEEPs) for the full passive antenna system at Ref. 2 when the reflector is included.

C Ports and Excitations

Let $\mathbf{a} \in \mathbb{C}^N$ denote the root-mean-square (rms) incident power-wave amplitudes at the N QOFN input ports (Ref. 2) generated by the AC outputs, so that $|a_p|^2$ equals the incident power at port p.

Varying the amplitudes and phases of the incident waves at the QOFN input ports using the PA module, we can combine the RF power into the output ports at Ref. 1 (power combining) and, simultaneously, form the required field distribution across the output ports to realize beam-steering (beamforming). This describes the joint power-combining and beamforming functionality. In the present work, we operate in a beamforming scenario where a single high-EIRP beam is electronically steered over the required angular sector by varying the amplitudes and phases of the incident waves determined using the beam-forming approach described below. The beam-steering limits are defined by hardware design (i.e., FPA geometry and reflector optics), which determine the gain loss in adjacent steering beams crossover and at the sector edges, and the practical calibration procedure for beamforming.

D Design Goals and Performance Metrics

We target electronic beamsteering over a few beamwidths (0.5° for 50 dBi-gain antenna) 2-D region, W-band operation (92–96 GHz), and EIRP ≥ 75 dBm.

Using sEEPs, the realized gain in direction (θ, ϕ) for excitation $\mathbf{a}$ can be written as [46]

$$G_{\mathrm{A}}(\theta,\phi) = \frac{2\pi}{\eta_0}\,\frac{\mathbf{a}^{\mathrm{H}}\mathbf{E}^{\mathrm{H}}(\theta,\phi)\,\mathbf{E}(\theta,\phi)\,\mathbf{a}}{\mathbf{a}^{\mathrm{H}}\mathbf{a}} \tag{1}$$

where the $1 \times N$ row vector $\mathbf{E}(\theta,\phi) = [\, e_1^{\mathrm{co}} \;\cdots\; e_N^{\mathrm{co}} \,]$ contains the copolar sEEPs, normalized to a 1 −W incident power wave at the excited port (rms convention), and η_0 is the free-space impedance. The total incident RF power at Ref. 2 is $P_{\mathrm{inc}} = \mathbf{a}^{\mathrm{H}}\mathbf{a}$. Thus, the corresponding EIRP is

$$\mathrm{EIRP}(\theta,\phi) = G_{\mathrm{A}}(\theta,\phi)\,P_{\mathrm{inc}}. \tag{2}$$

The EIRP is obtained by evaluating (2) with the available AC power $|a_p|^2 \le P_{\mathrm{sat},p}$.

Two practical constraints critically affect efficiency. First, the QOFN is not an isolated device. Therefore, strong mutual coupling effects between the array antenna elements can cause unwanted field interactions inside the QOFN and in the antenna aperture, which can lead to degraded performance [47]. When designed in isolation [48], the FPA shows < −24-dB mutual coupling levels, whereas in the present work, it is co-integrated with the QOFN, characterized by

$\mathbf{S}_{\text{FPA+QOFN}}$. Second, there should be a tight grouping of transmission coefficients from each QOFN input to a given output, allowing to minimize back-off levels between various ACs and thus maintaining maximum PA efficiency and system output power.

III. Beamsteering and EIRP Maximization for the Passive Antenna System

Beamforming is realized on the passive antenna system using the sEEPs. Because sEEPs include the effects of antenna mutual coupling and mismatch, they directly yield the excitation vector $\mathbf{a}$ (incident power waves at Ref. 2) required to form a beam in direction (θ, ϕ).

Let $\mathbf{E}(\theta, \phi)$ be defined as in (1). For an unconstrained maximum-gain solution at (θ, ϕ), the quadratic form in (1) is maximized by the conjugate-field matching (CFM) solution

$$\mathbf{a}_{\text{CFM}}(\theta, \phi) \propto \mathbf{E}^{\text{H}}(\theta, \phi) \tag{3}$$

that is, $a_p \propto (e_p^{\text{co}})^*$ when ports are equally weighted in power. In practice, the TX is configured to maximize EIRP, subject to per-channel limits. We therefore set the magnitudes to the available levels and align the phases for coherent combining

$$\begin{aligned} |a_p| &= \sqrt{P_{\text{sat},p}}, \quad \arg(a_p) = -\arg\left(e_p^{\text{co}}(\theta, \phi)\right) \\ p &= 1, \ldots, N \end{aligned} \tag{4}$$

which turns (2) into the beam-dependent EIRP with $P_{\text{inc}} = \sum_{p=1}^{N} P_{\text{sat},p}$. Here, P_{sat} is the maximum available incident power (PA saturated power) of each QOFN input.

IV. Beamsteering and EIRP Maximization for the Active Antenna System With a Transmitter

This section presents the beamforming/EIRP formulation for the complete active front end, defined in Fig. 1.

A. PA Module Model

The PA module is characterized at the small signal by $\mathbf{S}_{\text{PA}} \in \mathbb{C}^{(N+1)\times(N+1)}$, which is the cascade of the splitter ($\mathbf{S}_{\Delta}$) and N AC subblocks with states $q \in \{1, \ldots, Q\}$.[2] We index channels by $p \in \{1, \ldots, N\}$. For the PA module, the transmission coefficient from the splitter input (port $N+1$ at Ref. 3) to the pth AC output can be described by a single complex scalar that depends on the AC state q (we assume that the AC inputs are well-isolated through the input splitter):

$$t_p^{(q)} \triangleq (\mathbf{S}_{\text{PA}})_{p,\,N+1} \equiv T_{\text{PA}}^{(p,q)} \in \mathbb{C}.$$

Owing to the balanced high-PA (HPA) architecture, the passive output reflection coefficient of each AC, $\Gamma_p \triangleq (\mathbf{S}_{\text{PA}})_{pp}$, is nearly constant across q (see Section V-C); this stabilizes the interface toward Ref. 2. We adopt a reference state $q_0 = 129$ (maximum gain, zero phase) and collect the corresponding transmissions in the diagonal matrix

$$\mathbf{T}_{\text{PA}} \triangleq \text{diag}\left(t_1^{(q_0)}, \ldots, t_N^{(q_0)}\right).$$

Phase/amplitude deviations of other states are described by complex coefficients $c_{pq} = t_p^{(q)}/t_p^{(q_0)}$, incorporated later into a control vector $\mathbf{c}$.

[2]In our prototype $Q = 160$ (5-bit phase resolution with 5 amplitude states).

B. sEEPs With PA Module Interaction

Because the PA module is not reflectionless at Ref. 2, the interstage waves that enter the QOFN depend on the PA reflections $\{\Gamma_p\}$ and on $\mathbf{S}_{\text{Ant}}$ [49].

Consider the configuration in which only the channel p is active (set to q_0); all other channels are biased, such that their HPAs remain "ON" (to keep Γ_i fixed, i is the index across the ACs for a fixed p), while their DPAs are "OFF" (no drive) and PSs are in the state "0." For a scalar incident wave a_{in} at Ref. 3, the rms incident power-wave vector at Ref. 2 that results from driving the pth AC is $\mathbf{a}_{\text{ref}}^{p} \in \mathbb{C}^N$ and follows from the multiport connection equations:

$$\begin{aligned} (\mathbf{I} - \mathbf{\Gamma}\mathbf{S}_{\text{Ant}})\, \mathbf{a}_{\text{ref}}^{p} &= a_{\text{in}}\, t_p^{(q_0)}\, \mathbf{e}_p \\ \mathbf{\Gamma} &\triangleq \text{diag}(\Gamma_1, \ldots, \Gamma_N) \end{aligned} \tag{5}$$

where $\mathbf{e}_p$ is the pth standard basis vector. Provided the interface is well behaved, the matrix $(\mathbf{I} - \mathbf{\Gamma}\mathbf{S}_{\text{Ant}})$ is nonsingular, yielding the closed-form

$$\mathbf{a}_{\text{ref}}^{p} = a_{\text{in}}\, t_p^{(q_0)}\, (\mathbf{I} - \mathbf{\Gamma}\mathbf{S}_{\text{Ant}})^{-1}\, \mathbf{e}_p. \tag{6}$$

The system EEP associated with channel p and referenced to Ref. 3 is then defined by superposition

$$\left(e_{\text{sys}}^{\text{co}}\right)_p(\theta, \phi) = \sum_{i=1}^{N} \left(a_{\text{ref}}^{p}\right)_i\, e_i^{\text{co}}(\theta, \phi) = \mathbf{E}(\theta, \phi)\, \mathbf{a}_{\text{ref}}^{p}. \tag{7}$$

Combining these into the row vector gives

$$\mathbf{E}_{\text{sys}}(\theta, \phi) \triangleq \left[\, \left(e_{\text{sys}}^{\text{co}}\right)_1 \;\cdots\; \left(e_{\text{sys}}^{\text{co}}\right)_N \,\right]$$

which includes all PA-to-antenna interactions at the reference state q_0. In practice, we observe that, thanks to the nearly q-invariant Γ_p, the shapes of $(e_{\text{sys}})_p$ do not change with the channel state. Thus, for $q \neq q_0$, the change is modeled by a complex scaling c_{pq}.

Strong coupling effects and nonzero Γ_p perturb the passive antenna system sEEPs [49] and can, through (5), create unwanted field interactions in the QOFN that vary with excitation (beamforming/beamsteering). The above formulation inherently accounts for these effects because $\mathbf{E}_{\text{sys}}$ is constructed from the scattering parameters of the system components.

C. Active Antenna Beamforming

Let the AC control vector be $\mathbf{c} = [\, c_1, \ldots, c_N \,]^{\text{T}} \in \mathbb{C}^N$, where each c_p represents the complex state of pth AC relative to q_0 (continuous in this section; quantization is handled below). For a given beam direction (θ, ϕ) the radiated field from the full active front end is $\mathbf{E}_{\text{sys}}(\theta, \phi)\,\mathbf{c}$.

The system realized gain and EIRP, both referred to Ref. 3, follow the same quadratic-form structure as in (1) and (2) [50]

$$G_{\text{sys}}(\theta, \phi) = \frac{2\pi}{\eta_0}\, \frac{\mathbf{c}^{\text{H}}\mathbf{E}_{\text{sys}}^{\text{H}}(\theta, \phi)\,\mathbf{E}_{\text{sys}}(\theta, \phi)\,\mathbf{c}}{|a_{\text{in}}|^2\, \mathbf{c}^{\text{H}}\mathbf{T}_{\text{PA}}^{\text{H}}\mathbf{T}_{\text{PA}}\mathbf{c}} \tag{8}$$

$$EIRP_{\text{sys}}(\theta, \phi) = \frac{2\pi}{\eta_0}\, \mathbf{c}^{\text{H}}\mathbf{E}_{\text{sys}}^{\text{H}}(\theta, \phi)\,\mathbf{E}_{\text{sys}}(\theta, \phi)\,\mathbf{c} \tag{9}$$

where $\mathbf{T}_{\text{PA}} = \text{diag}(t_1^{(q_0)}, \ldots, t_N^{(q_0)})$ and $|a_{\text{in}}|^2\, \mathbf{c}^{\text{H}}\mathbf{T}_{\text{PA}}^{\text{H}}\mathbf{T}_{\text{PA}}\mathbf{c}$ equals the total incident RF power at Ref. 2. The forms in (8) and (9) are the direct active-system counterparts of (1) and (2).

1) Unconstrained Maximum-Gain Solution: Maximizing $G_{\text{sys}}(\theta, \phi)$ with respect to $\mathbf{c} \neq \mathbf{0}$ yields the generalized eigenvalue problem

$$\mathbf{E}_{\text{sys}}^{\text{H}} \mathbf{E}_{\text{sys}}\, \mathbf{c}_{\text{opt}} = \lambda_{\max}\, \mathbf{T}_{\text{PA}}^{\text{H}} \mathbf{T}_{\text{PA}}\, \mathbf{c}_{\text{opt}}. \tag{10}$$

If $\mathbf{T}_{\text{PA}} \propto \mathbf{I}$ (well-equalized AC magnitudes), (10) reduces to a conjugate-field match on the system EEPs, that is, $c_p \propto (e_{\text{sys}}^{\text{co}})_p^*$, consistent with the passive-only CFM solution.

2) EIRP Maximization Under Per-Channel Limits: In the TX, the relevant constraint is the available per-channel power at Ref. 3. To maximize the EIRP, we set each AC for maximum output power ($P_{\text{sat},\ p}$), achieved by setting $|c_p| = 1$ and increasing $|a_{\text{in}}|$. Owing to the negligible AM–PM conversion of the PA chain, the EIRP-maximizing phase can be obtained from a small-signal solution

$$\arg c_p = -\arg\left(\left(e_{\text{sys}}^{\text{co}}\right)_p\right), \quad p = 1, \ldots, N. \tag{11}$$

If thermal or linearity margins require derating, we replace $P_{\text{sat},p}$ by the chosen operating power. The resulting $\mathbf{c}$ is then projected onto the discrete AC state set by nearest-neighbor quantization in angle and magnitude.[3]

In this work, a 5-bit phase resolution is employed. Such resolution is generally sufficient to avoid noticeable far-field degradation in phased-array systems [51]. For the proposed FPA architecture, full-wave simulations show that 5-bit phase quantization combined with up to 2-dB amplitude imbalance results in <0.1-dB peak realized-gain reduction for the synthesized reflector antenna beams. This limited sensitivity is a consequence of the usage of the QOFN. In the present design, beam switching is achieved through the excitation with the incident power waves with substantially different phases at the QOFN inputs. The reflector and the FPA, in turn, determine the beam-steering angle when different FPA elements are excited. Therefore, the FPA + QOFN-based architecture relaxes the phase-accuracy requirements compared to conventional phased arrays, while preserving beam shape and steering precision within the targeted range (see Section VII-B).

The practical procedure that implements this formulation on the measured data is provided in Section VII-A.

V. Antenna System Design

A. Reflector Geometry

Dual-reflector configurations can provide high antenna gain owing to a large effective focal length [6], [52], but at the W-band, their mechanical complexity is significant. Additionally, in our system (Section II), the QOFN and PA module are co-located in the front end; the required volume would introduce considerable blockage in an axisymmetric reflector configuration. We therefore utilize a single offset parabolic reflector as a tradeoff between EM performance and implementation complexity.

In addition, compliance with the ETSI Class 3 sidelobe mask defined in the horizontal plane ($\phi = 90°,\ 270°$) is an important design constraint. Conventionally, deep reflector optics ($F/D_{\text{r}} \leq 0.25$) are preferred for sidelobe suppression (e.g., in hat-feed designs [53]), however, small F/D_{r} increases beam scan loss [54], [55], [56]. In contrast, $F/D_{\text{r}} \geq 0.5$ requires a larger FPA for optimum illumination [57].

[3]When quantization is significant, one may optionally re-optimize $\mathbf{c}$ on the discrete grid via a small local search to recover the coherent-combining loss.

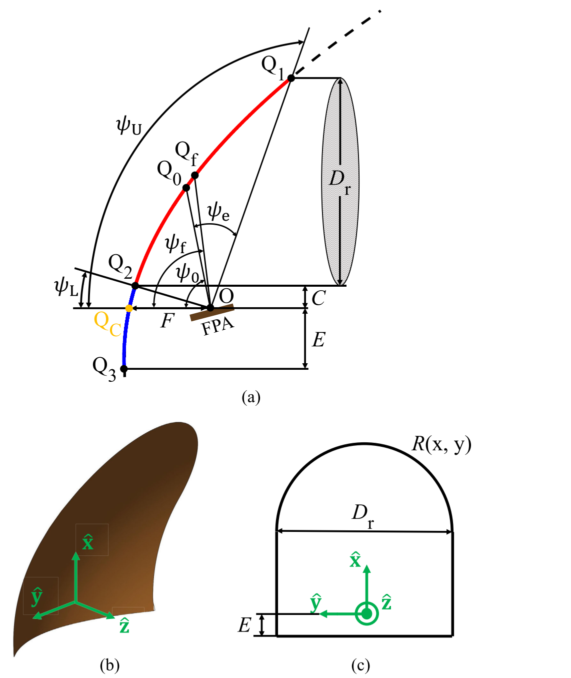

Fig. 2. Offset reflector with rim extension: (a) profile (not to scale), (b) 3-D surface, and (c) rim outline. Notation: projected diameter D_{r}, focal length F, half-subtended angle ψ_{e}, rim-bisector angle ψ_0, feed steering angle ψ_{f}, clearance C, extension E. Geometry: $D_{\text{r}} = 0.4$ m, $\|Q_1 Q_2\| \approx 0.49$ m, $F = 0.14$ m, $\|Q_C Q_2\| = C = 5$ mm, $\|Q_2 Q_3\| = 20$ mm, $E = 15$ mm, $\psi_U = 111°$, $\psi_0 = 56°$, $\psi_L = 1°$, $\psi_{\text{e}} = 55°$, and $\psi_{\text{f}} = 70.4°$.

Balancing these competing effects, we select $F/D_{\text{r}} = 0.35$ as a compromise between scan capability and sidelobe level (SLL) performance.

Following standard offset reflector design procedures [55], [58], [59], [60], the geometry is defined as in Fig. 2. For the W-band P2P backhaul case, a ≥ 50-dBi antenna is required to compensate for a high path loss; we choose a projected diameter $D_{\text{r}} = 400$ mm = 0.4 m, yielding a theoretical maximum directivity of 51.9 dBi at 94 GHz. With $F/D_{\text{r}} = 0.35$, the focal length is $F = 140$ mm. A clearance $C = 5$ mm avoids front-end blockage while keeping the antenna compact, based on its size evaluation in [48]. The half-subtended angle ψ_{e}, the feed pointing angle ψ_{f}, and the rim-bisector angle ψ_0 follow [55]. The baseline profile is shown in Fig. 2(a).

Asymptotic analysis, using physical optics (POs) with physical theory of diffraction (PTD) in GRASP, is employed to optimize the offset geometry for maximum directivity under a −10-dB rim taper (Gaussian feed model). The resulting baseline reflector achieves $D = 50.1$ dBi. However, high far-out sidelobes (FSLs) remain in the back region due to direct feed radiation and edge diffraction [see $\theta \in [90°, 180°]$ in Fig. 3(a)], so, similar to [61], we extend the rim as in Fig. 2(a) and (c) (segment $Q_2 Q_3$), producing the 3-D surface in Fig. 2(b) to block direct feed radiation in the backward region. The modified rim outline R can be expressed piecewise

$$R: \begin{cases} \left(x - \left[\dfrac{D_{\text{r}}}{2} + C\right]\right)^2 + y^2 = \dfrac{D_{\text{r}}^2}{4}, & x > \left(\dfrac{D_{\text{r}}}{2} + C\right) \\ y = \pm\dfrac{D_{\text{r}}}{2}, & -E < x \leq \left(\dfrac{D_{\text{r}}}{2} + C\right) \\ x = -E, & |y| \leq \dfrac{D_{\text{r}}}{2} \end{cases} \tag{12}$$

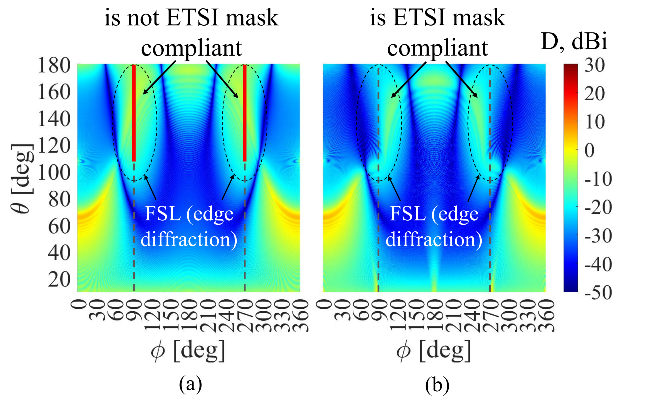

Fig. 3. Far-field patterns (co-pol. for $\theta \in [5°; 180°]$) of the offset reflector antenna when illuminated by the Gaussian feed with a −10-dB rim taper: (a) baseline circular rim and (b) extended rim. Dashed lines: horizontal cuts; red lines indicate the angles where the ETSI mask is not compliant.

where E is the vertical extension (see Fig. 2). With this extension, FSLs are strongly suppressed for the horizontal plane [$\phi = [90°, 270°]$; see Fig. 3(b)], enabling ETSI mask compliance while keeping the overall dimension <60 cm.

B. FPA With Integrated QOFN

We implement an integrated FPA + QOFN module tailored to electronic beamsteering of 0.65° from boresight in any azimuth direction (i.e., 1° 2-D scanning range) using WG technology. Beamsteering is achieved through the desired excitation of the FPA elements. The main functional parts of the module are shown in Fig. 4:

1) M-element FPA, responsible for shaping the reflector illumination and enabling controlled beamsteering.
2) N-input-M-output QOFN, performing joint spatial power combining and beamforming.
3) Rectangular WG QOFN-to-FPA interface.
4) Input rectangular WG and ridge WG (RWG) fan-in network interfacing the QOFN with the PA module (see Section VI-A).
5) Curved absorber blocks integrated into the PPWG region to suppress internal reflections and stabilize the quasioptical field distribution.

1) FPA and Element Decoupling: The FPA design is adopted from [48]: it is a seven-element open-ended rectangular WG array surrounded by aperture pins for element-level pattern shaping and element decoupling (mutual coupling level is < −24 dB), and a perforated choke-ring pair provides array-level beam shaping. The radiation efficiency is 94%–98% across elements. Thus, this FPA, initially designed in isolation, is co-integrated with the QOFN with a jointly optimized interface. It is also worth noting that the scanning range can be improved by adding more elements, as in [62] (see Section VIII).

2) QOFN Physical Architecture: The QOFN follows the concept of unified spatial power-combining and beamforming described in [38]. It comprises a PPWG region bounded by two circular walls of radii R_1 and R_2. The N inputs $I_1, \ldots, I_N$ (along R_1) are implemented as open-ended RWGs that "radiate" into the PPWG region, enabling compact interelement spacing. The M outputs $O_1, \ldots, O_M$ (along R_2) are implemented as H-plane

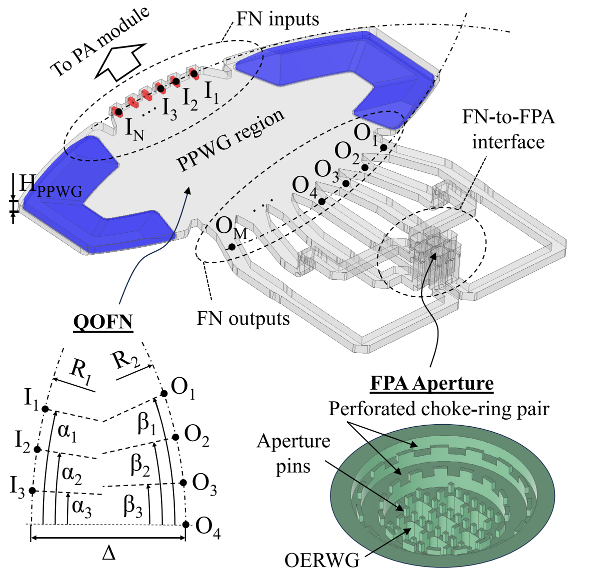

Fig. 4. Main parts of the integrated FPA + QOFN module. Here, $N = 6$ (number of the QOFN inputs) and $M = 7$ (number of the QOFN outputs and the FPA elements). Here, $\alpha_1 = 5.83°$, $\alpha_2 = 3.18°$, and $\alpha_3 = 1.06°$ are the angles corresponding to the input ports positions along $R_1 = 70$ mm, $\beta_1 = 11.65°$, $\beta_2 = 7.44°$, and $\beta_3 = 3.71°$ are the angles corresponding to the output ports positions along $R_2 = 69.6$ mm, the separation $\Delta = 30$ mm, and the PPWG height $H_{\mathrm{PPWG}} = 1.27$ mm.

sectoral horns to improve directivity[4] [see [38], (3)] of the QOFN and are connected to the FPA ports. Curved absorber blocks are placed along the PPWG sidewalls to suppress multiple internal reflections. The vertical dimensions of all WG cross sections (heights) are chosen to be 1.27 mm. The principal dimensions of the synthesized structure are given in Fig. 4, whereas the detailed implementation with dimensions is shown in Section VI-A. In this work, we use $N = 6$ inputs and $M = 7$ outputs, a practical choice on the IC count and the number of FPA elements.

3) Numerical Synthesis and Optimization: The co-integrated FPA + QOFN module was synthesized numerically using a dedicated PPWG radiation model with input and output WG apertures together with the full-wave simulation in Ansys HFSS with absorbing boundary conditions along the walls to define the baseline configuration (e.g., R_1, R_2, input/output port spacing and widths, ridge heights, PPWG gap, and horn flare/length), with the FPA radiating aperture held fixed. Accordingly, the optimization targets the QOFN geometry and the QOFN-to-FPA interface (transition geometry) to maximize the realized gain G_A [(1), and its CFM solution in Section III]. For the reflector/FPA used here, the optimum excitation for a beam corresponding to the peaks of sEEPs is dominated by a single FPA element (located at the center of the focal spot), while the surrounding elements have a relative field taper below −15 dB. Therefore, a first-order objective targets maximum realized gain for these beams. Effectively, this is equivalent to having the QOFN optimization goal of achieving a maximum power-combining efficiency (see [38]) for each output port.

The final design was obtained through fine-tuning of the baseline configuration with the following included features:

[4] In this context, for the utilized QOFN, the directivity is a measure of the QOFN's ability to isolate a wanted and unwanted coupling to the output ports.

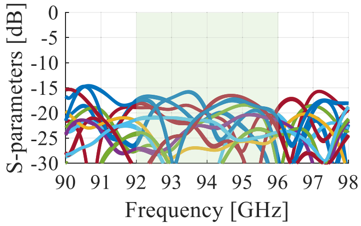

Fig. 5. Simulated S-parameters of the FPA + QOFN module input ports.

curved absorber blocks, the side field reflectors for the edge input RWG elements, and the side width steps for the edge output WG elements (see Fig. 6). Here, the material of the curved tapered magnetic absorber blocks is C-RAM RGD-124 from Cuming Microwave (ε = 16.83, μ = 0.77, $\tan\delta_\varepsilon$ = 0.1331, and $\tan\delta_\mu$ = 0.0519), which is suitable for the CNC machining and demonstrates sufficient EM energy absorption, comparable to [63], in the W-band. The absorber blocks are located in the sidewall region of the PPWG regions to absorb diffracted EM waves, thus suppressing multiple PPWG reflections. For metallic parts, aluminum is chosen as the material with the surface roughness of 0.4 μm extracted from the WG section measurements and included in the Groiss model as the parameter for the simulations. The optimization included additional beamsteering directions, such as the crossover point directions of the sEEPs.

4) Port Coupling and Isolation: The coupling characteristics between the QOFN input ports are illustrated in Fig. 5. As observed, the off-diagonal $|\mathbf{S}_{ij}|$ levels remain below approximately −16 dB across the operating band, which is attributed to the design of the QOFN input port. This reduces the sensitivity of the synthesized excitations to channel-to-channel perturbations and enables stable beam synthesis.

5) Beam Synthesis and Aperture Efficiency: The approach for evaluating the performance involves computing the pEEPs of the FPA + QOFN in Ansys HFSS; we use them as a feeding source to obtain the sEEPs in GRASP (TICRA) at Ref. 2. Using the sEEPs as $e_p^{\mathrm{co/cx}}$ and (1) and (2) in Section II, we obtain excitations for multiple beam directions, corresponding to the on-axis and off-axis beams.

Fig. 6 shows the instantaneous fields in the FPA + QOFN module and resultant far-field patterns, which were computed for the excitation scenarios for two beam directions: $\theta_s = 0°$ (beam #1) and $\theta_s = 0.65°$, $\varphi_s = 150°$ (beam #7), which correspond to the mainlobes of the sEEPs at Ref. 1, when feeding the reflector with the standalone FPA. Thus, one can observe the propagating field focusing toward the output connected to the central element (which has dominant excitation for the beam #1) [Fig. 6(a)] and the most offset element (which has dominant excitation for the most scanned beam #7) [Fig. 6(b)], respectively.

As expected for $N < M$ (see Section VIII, and [38]), leakage to adjacent FPA elements appears, producing small distortions relative to the reference FPA far-field patterns [Fig. 6(c) and (d)]. The decomposition of the total aperture efficiency into spillover, polarization, amplitude, and phase subefficiencies (see definitions here [57]), $e_{\mathrm{ap}} = e_{\mathrm{sp}}\, e_{\mathrm{pol}}\, e_{\mathrm{amp}}\, e_{\mathrm{ph}}$, indicates an overall ≈ 0.6-dB degradation for the FPA + QOFN-illuminated reflector relative to the standalone FPA (with an ideal feeding network), caused primarily by phase subefficiency loss (~0.2 dB; see Fig. 7).

TABLE I

Ohmic Loss Budget for the FPA + QOFN Module at 94 GHz for Beam #1 (Best Case), and Beam #7 (Worst Case)

FPA+QOFN module part	**Beam #1 (dB)**	**Beam #7 (dB)**
PPWG region (excluding absorber loss)	0.25	0.25
Ridge WG fan-in	0.30	0.30
Input rectangular WG fan-in and QOFN-to-FPA interface	0.30	0.30
FPA	0.20	0.20
Absorber blocks	0.85	2.25
Total ohmic loss (dB)	**1.90**	**3.30**

Notes: The mismatch effects (reflection coefficients) are not included.

6) Beam-to-Beam Coupling: The coupling between the synthesized beams can be evaluated through the beam-overlap (or pattern-overlap) integral formulation [49], where the coupling level is determined by the inner product of the beam far-field patterns. For directive beams, as is the case for this work, the beam-to-beam coupling is mainly attributed to the overlap of the mainlobes of the synthesized beams. At the same time, the latter corresponds to the mainlobes of the sEEPs (Ref. 1). Consequently, the inner product of two sEEPs (Ref. 1) is proportional to the real part of the mutual impedance of the corresponding FPA elements. Therefore, the beam-to-beam coupling is dominated by the mutual coupling between these elements, which is in the worst case scenario < −24 dB.

In the present implementation, the finite directivity of the QOFN ($N < M$) results in residual leakage toward adjacent output ports at levels up to approximately −13 dB. This leakage slightly increases the effective pattern-overlap between adjacent synthesized beams. Based on the measured radiation patterns, the normalized overlap between the on-axis beam (beam #1) and its adjacent off-axis beam (beam #7) increases, from 0.1 to 0.27. Although measurable, this increase remains moderate and does not lead to observable distortion of the beam shapes within the targeted steering sector. This is confirmed by the results provided in Section VI-C and in Fig. 6.

7) Insertion Loss: The QOFN insertion loss for the present implementation varies between 2.3 and 3.7 dB for the on-axis and off-axis beam excitation scenarios, respectively, where the upper loss value occurs for beam #7 excitation (the edge QOFN output), which is mainly attributed to a PPWG field "grating lobe" (GL) being excited toward the absorber block [see Fig. 6(b)]. Table I demonstrates the ohmic loss budget for the FPA + QOFN module for two beams, representing the upper and lower bounds. As seen, the losses fall within the range reported for similar QO structures, that is, Rotman lenses [42], and are acceptable considering the typical state-of-the-art W-band technology, where a switching IC usually has over 3-dB loss per one SPDT (single pole double throw) switching cascade [44], [64], therefore, eliminating it is beneficial. Moreover, the optimized QOFN has well-grouped transmission coefficients to each output with up to ±1.5-dB magnitude variation between the inputs. This allows for optimal PA module operation in terms of output power and efficiency when aiming at the maximum system EIRP.

C. PA Module

The PA module provides the amplitude and phase control required to excite the $N = 6$ QOFN inputs and facilitates high

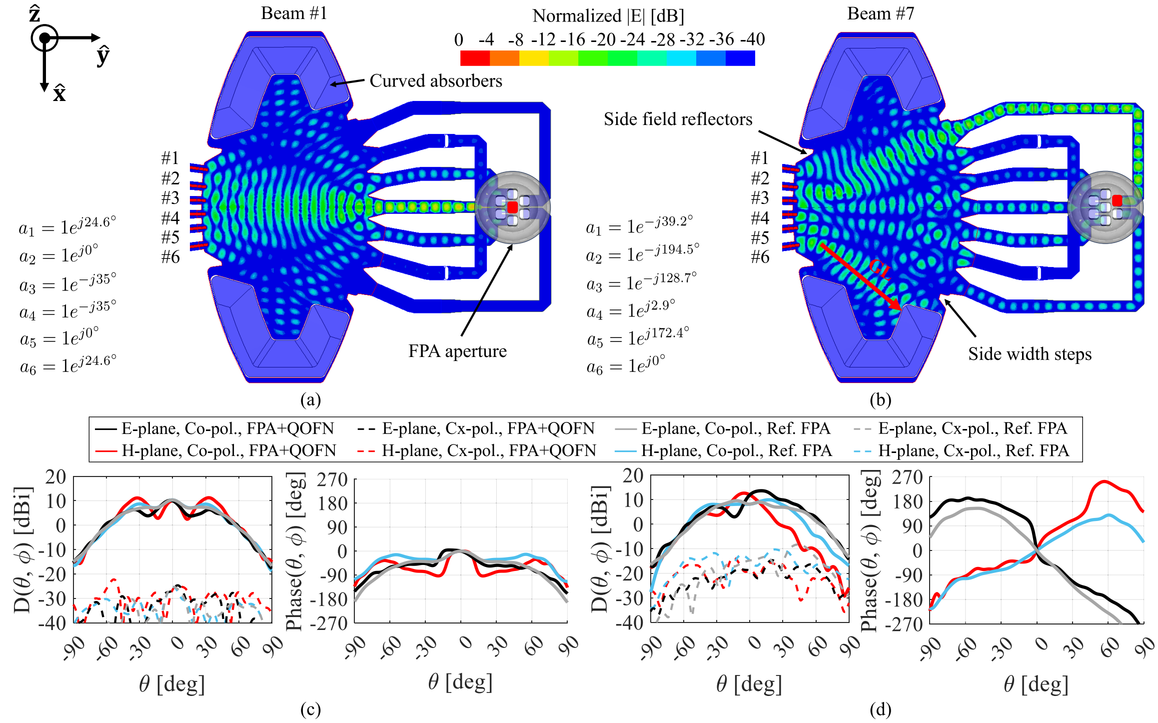

Fig. 6. QOFN operating principle. (a) and (b) Instantaneous E-field in the parallel plate WG and input excitations **a** [from (4)] for on-axis beam #1 and off-axis beam #7 and (c) and (d) corresponding simulated amplitude/phase FPA pEEPs (Ref. 1) and FPA + QOFN far-field pattern (Ref. 2). Here, GL is the grating lobe.

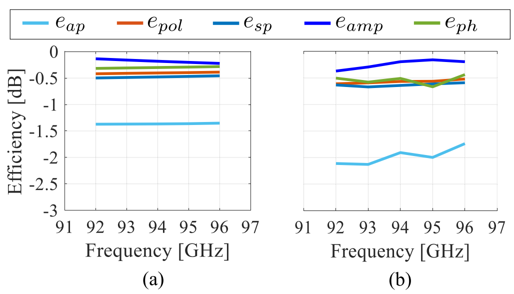

Fig. 7. Simulated beam #1 efficiencies for the offset reflector antenna, when illuminated by (a) FPA (Ref. 1) and (b) FPA + QOFN (Ref. 2).

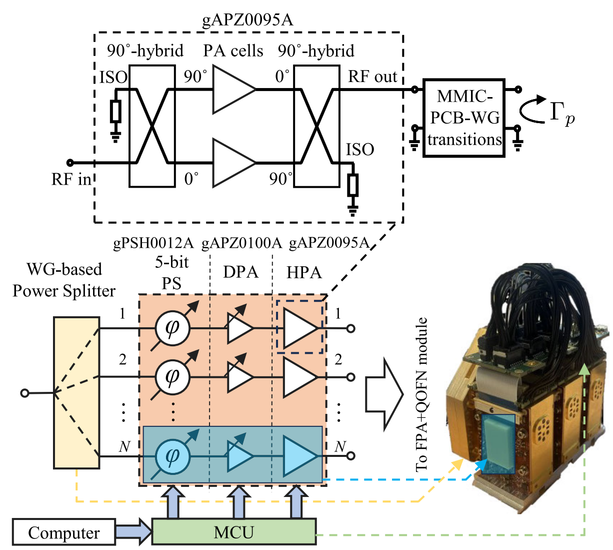

Fig. 8. PA module block diagram and photograph with $N = 6$ ACs (see Fig. 1).

output power. It comprises a WG N-way splitter and N ACs, each consisting of three monolithic microwave ICs (MMICs) [26], [65], [66] in 100-nm GaAs pHEMT developed by Gotmic AB as shown in Fig. 8. Here, a 5-bit PS (gPSH0012A) facilitates 11.25° phase shift discrete with ±23° maximal phase error (typical rms phase error is 8°) and ±1-dB maximal amplitude variation (typical rms amplitude error is 0.5 dB) [65]. The PS provides ≈ 16-dB insertion loss and ≤ −8-dB input/output reflection coefficient. A DPA (gAPZ0100A) operates in a small-signal mode and can achieve the gain of ≈15dB, to compensate for the PS loss. The gain can be adjusted by changing the DPA drain bias. The small-signal input/output reflection coefficient ≤ 10 dB [66].

In turn, a balanced high-power PA (gAPZ0095A [26], HPA) is a crucial component of the presented system. Inset in Fig. 8 shows the principal block diagram of the balanced PA architecture. The design comprises two quadrature hybrids in the input and output. The input hybrid forms two quadrature components that are amplified in the PA cells and combined in the output hybrid. The hybrids buffer PA cells from the reflective components connected to the input and output, thereby reducing the sensitivity of the PA to the load impedance (mitigating load-pull effects) and improving the input and output reflection coefficients. Furthermore, the combined power of the PA cells, particularly ≈27 dBm, can be achieved in the output that is relevant for high-EIRP systems. In the developed PA module, PS + DPA are isolated from the AC output by the HPA, which is always "ON" at a fixed quiescent bias point. Γ_p of each PA module is therefore determined by its HPA, independent of the selected phase/gain state. Turning PS/DPA "OFF" during calibration will yield the same Γ_p and therefore have an impact on the overall excitation

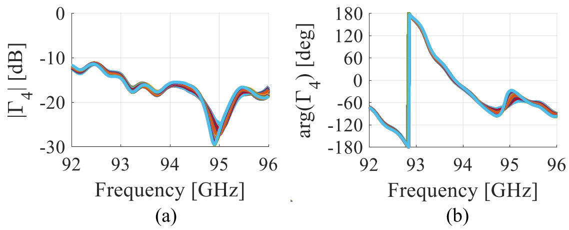

Fig. 9. Measured PA module: (a) magnitude and (b) phase of the small-signal output reflection coefficient for AC #4 across all states.

TABLE II

PA MODULE: TYPICAL† MEASURED AC PERFORMANCE

Maximum gain $G_{\max}$	10 dB
Output power at 1 dB comp. $P_{1\text{dB}}$	24 dBm
Saturated output power P_{sat}	> 26 dBm
Amplitude control range / resolution	6 dB / 1.2 dB
Phase resolution	5 bit
RMS phase error	10°
Switching delay	≤ 1 ms
Input/Output return loss (passive)	≤ -10 dB

Notes: † The typical values provided due to the slightly different performance of AC channels.

at Ref. 2 just as it would when all channels are "ON" under normal use. Therefore, the HPA provides good (≤ -20 dB) and nearly state-invariant (amplitude change ≤ 0.8 dB, phase change $\leq 6°$ at 94 GHz as seen in Fig. 9) output matching while the device is "ON," which is beneficial for calibration and reduces reflections at the QOFN interface [26]. It is worth noting that the output reflection coefficient (Fig. 9) remains stable for all power levels.

The above-described MMICs are mounted on a single PCB including the orthogonal probes to the rectangular WG interface forming an AC. Typical value of the resultant AC small-signal gain is 10 dB with continuous amplitude control. In this work, we consider 6-dB amplitude control range with 1.2-dB steps (5 gain states). The achieved combined power at the module output is 30–32 dBm, which corresponds to the 1-dB-compression point. This is sufficient for the $\geq$ 75-dBm peak EIRP accounting for the reflector and QOFN losses shown above. AC states are set through a main control unit board with a serial USB interface to MATLAB.

The main performance metrics for the PA module are summarized in Table II.

VI. Passive Antenna System: Implementation, Measurement, and Performance

A. Antenna Fabrication and Assembly

The integrated FPA + QOFN module is realized using three aluminum H-plane WG split-blocks (Fig. 10): Layer #1 is the FPA radiating aperture [48]. Layer #2 is a WG fan-out that: 1) provides orthogonal interlayer transitions from the FPA elements and 2) serves as a lid for the QOFN PPWG region. Layer #3 implements the QOFN, following the design procedure outlined in Section V-B. In addition, Layers #2 and #3 include the two-section transition from the customized WG element (2.1 × 1.27 mm) to the QOFN output ports. Key dimensions and port placement are shown in Fig. 10(a) and (b), with the mechanical assembly in Fig. 10(c).

The fabricated reflector and the FPA + QOFN module are shown in Fig. 11(a) and (b), where the complete prototype of the passive antenna system is installed in the anechoic chamber. The reflector (Section V-A) is CNC-machined, polished, and mounted using an adapter fixture. Small filets are added along the rim to reduce edge diffraction contributions to the far-field, and stiffening ribs on the back preserve surface shape (Fig. 11).

B. Measurement Setup and Procedure

Measurements are performed in the Chalmers anechoic chamber configured as a compact-antenna–test range (CATR) with a quiet zone of 550 mm [Fig. 11(c)]. For preliminary alignment, the input port #3 [Fig. 6(b)] is driven, and the reflector elevation/tilt and the FPA + QOFN module position are adjusted to match the measured and simulated H-plane cuts near boresight. After alignment, sEEPs referenced to Ref. 2 are measured over $|\theta| \leq 5°$ with fine angular resolution and $\varphi \in [0°, 345°]$ in 15° steps. For ETSI mask verification, full H-plane cuts are measured at different incident power levels (higher input power level for $5° < |\theta| \leq 180°$ concatenated with low input power level sEEPs for $|\theta| \leq 5°$) to facilitate the required dynamic range.

C. Passive Antenna System Performance

Fig. 12(a) compares simulated and measured passive reflection coefficients $(\mathbf{S}_{\text{Ant}})_{ii}$ at the N inputs (Ref. 2). One can observe that $|(\mathbf{S}_{\text{Ant}})_{ii}| \leq -14$ dB across 92–96 GHz with good agreement. The active (scan) reflection coefficients (computed for the optimized excitations) satisfy $|\Gamma_{\text{act}}| < -10\,\text{dB}$ for the majority of the beams [Fig. 12(b)], except for the peaks up to ≤ -8 dB for beam #1, ports I_3 and I_4; beams #2, #5, ports I_2, I_5; beams #6, #7, ports I_1, I_6 (see definitions for beams in the caption for Fig. 13).[5] Nevertheless, it does not significantly affect the PA module performance, owing to the balanced architecture of the HPA.

Using (1) and (2) with the measured sEEPs $e_p^{\text{co/cx}}(\theta, \phi)$, we synthesize seven beams (beams #1–#7), where their directions coincide with the mainlobes of the reflector sEEPs (Ref. 1). Fig. 13 shows simulated and measured far-field patterns (Ref. 2), with the ETSI Class 3 mask for the E-band. We observe that within $\theta \in [-180°, 180°]$, all beams are compliant except for <1 dB peaks at ±103° caused by the edge diffraction on the reflector rim. These peaks can be eliminated by covering part of the rim with absorptive material. The peak realized-gain differences between the measurements and simulations are within 0.8 dB as seen in Fig. 14.

VII. Active Antenna System Performance: Beamsteering and EIRP

A. Experimental Procedure (Per Frequency Point)

1) *Measure the PA Module:* acquire $\mathbf{S}_{\text{PA}}$ (splitter + ACs) with all ACs biased (or a fraction of it) and extract $t_p^{(q)} = (\mathbf{S}_{\text{PA}})_{p,N+1}$ and the output passive reflection coefficients (nearly q-invariant) $\Gamma_p = (\mathbf{S}_{\text{PA}})_{pp}$ for all p [see (5)]. Define the reference-state transmission matrix $\mathbf{T}_{\text{PA}} = \text{diag}(t_1^{(q_0)}, \ldots, t_N^{(q_0)})$.

[5] For an incident vector $\mathbf{a}$ at Ref. 2, the active reflection at port i is $\Gamma_{\text{act }i} = \sum_{j=1}^{N} S_{ij}\, a_j / a_i$, evaluated per beam.

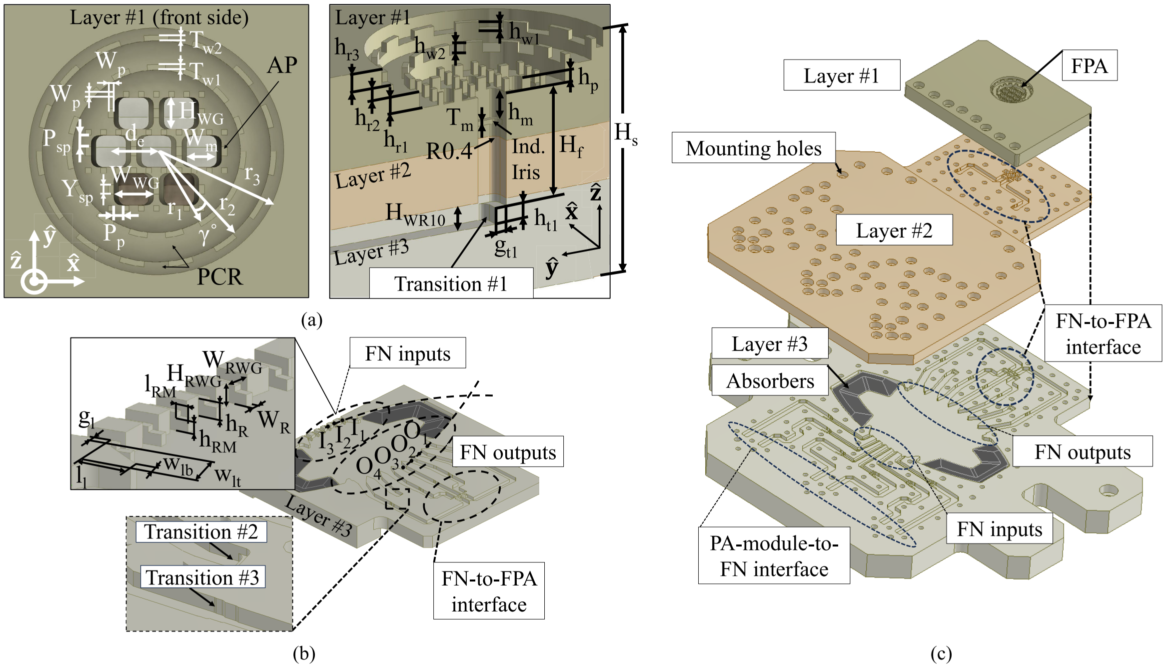

Fig. 10. FPA + QOFN design implementation: (a) FPA aperture, (b) QOFN layout, and (c) mechanical assembly. Here, $N = 6$ (QOFN inputs) and $M = 7$ (FPA elements), consistent with Fig. 1. The main geometrical parameters (mm): $H_s = 13$, $H_{WG} = 1.74$, $d_e = 2.4$, $h_{r1} = 0.9$, $h_{r2} = 0.6$, $h_{r3} = 0.95$, $h_{w1} = 0.55$, $h_{w2} = 0.5$, $h_p = P_{sp} = 0.64$, $h_m = 1.52$, $T_m = 0.25$, $P_p = Y_{sp} = 0.5$, $W_{WG} = 2.1$, $W_m = 1.6$, $\gamma = 12^\circ$, $T_{w1} = T_{w2} = W_p = 0.3$, $r_1 = 4.45$, $r_2 = 6.05$, $r_3 = 6.75$, $H_f = 5.92$, $h_{t1} = 0.85$, $g_{t1} = 0.65$, $l_l = 2.8$, $w_{lb} = 0.7$, $w_{lt} = 3$, $g_l = 0.5$, $l_{RM} = 0.74$, $h_{RM} = 0.63$, $h_R = 0.925$, $W_{RWG} = 1.525$, $H_{RWG} = H_{PPWG} = H_{WR10} = 1.27$, and $W_R = 0.48$.

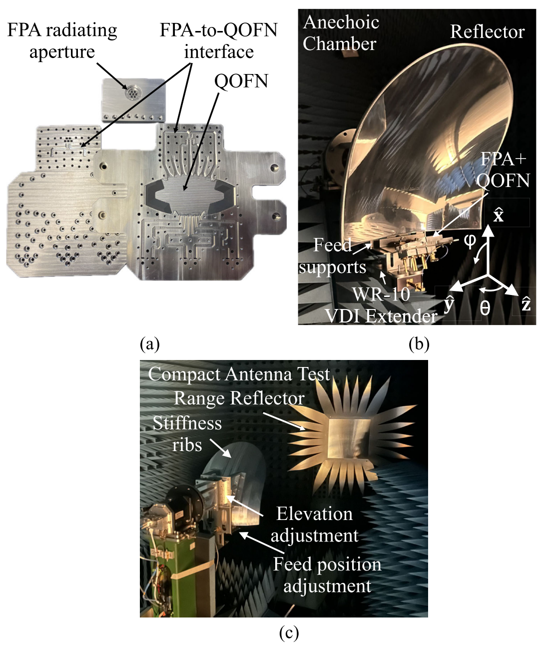

Fig. 11. Fabricated prototypes of the passive antenna system: (a) FPA + QOFN module, (b) reflector prototype with the FPA + QOFN mounted in the anechoic chamber, and (c) measurement setup (CATR).

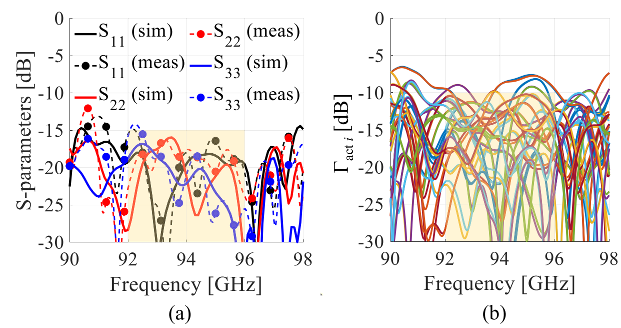

Fig. 12. (a) Simulated and measured passive S-parameters of the FPA + QOFN and (b) synthesized beam active reflection $|\Gamma_{\mathrm{act}\ i}|$ at Ref. 2.

2) *Measure the Passive Antenna System:* acquire $\mathbf{S}_{\mathrm{Ant}}$ (FPA + QOFN) and the sEEPs $\{e_p^{\mathrm{co}}(\theta,\phi)\}$ at Ref. 2.
3) *Synthesize Beams (Optimum Beamforming):* a) use (6)and (7) to form $\mathbf{E}_{\mathrm{sys}}(\theta,\phi)$; b) for maximum realized gain, solve the generalized eigenvalue problem (10) to obtain $\mathbf{c}_{\mathrm{opt}}$; and c) for EIRP-limited operation, adjust phases/magnitudes using (11) and round-off $\mathbf{c}$ to the nearest AC states $\{q_p\}$ (update $c_p \leftarrow t_p^{(q_p)}/t_p^{(q_0)}$).
4) *Evaluate Metrics:* compute $\mathrm{EIRP}_{\mathrm{sys}}(\theta,\phi)$ and $G_{\mathrm{sys}}(\theta,\phi)$ for the synthesized beams using (8) and (9).

1) Block Connection and Calibration: The interconnection of the system blocks used during calibration is shown in Fig. 1. For $\mathbf{S}_{\mathrm{Ant}}$, we used the simulated results, owing to a good agreement with the measurement results. For validation of the procedure described above, we cascade the measured PA module S-matrix $\mathbf{S}_{\mathrm{PA}}$ (splitter + ACs) with the simulated S-matrix $\mathbf{S}_{\mathrm{Ant}}$ (FPA + QOFN), thus including realistic AC behavior and 5-bit phase resolution in the analysis. We define $t_p^{(q)} \triangleq (\mathbf{S}_{\mathrm{PA}})_{p,N+1}$ (transmission from the splitter input at Ref. 3 to AC output p in state q) and $\Gamma_p = (\mathbf{S}_{\mathrm{PA}})_{pp}$ (AC output reflection). Owing to the balanced architecture of the HPA, Γ_p is nearly invariant to the channel state q (see Section V-C). A reference state $q_0 = 129$ (maximum gain, 0° phase) is used to form $\mathbf{T}_{\mathrm{PA}} = \mathrm{diag}(t_1^{(q_0)},\ldots,t_N^{(q_0)})$. The $T_{\mathrm{PA}}^{(p,q)} = t_p^{(q)}$ values are measured channel-by-channel in a 2-port regime (Fig. 8) with all standby ACs biased on and terminated with matched

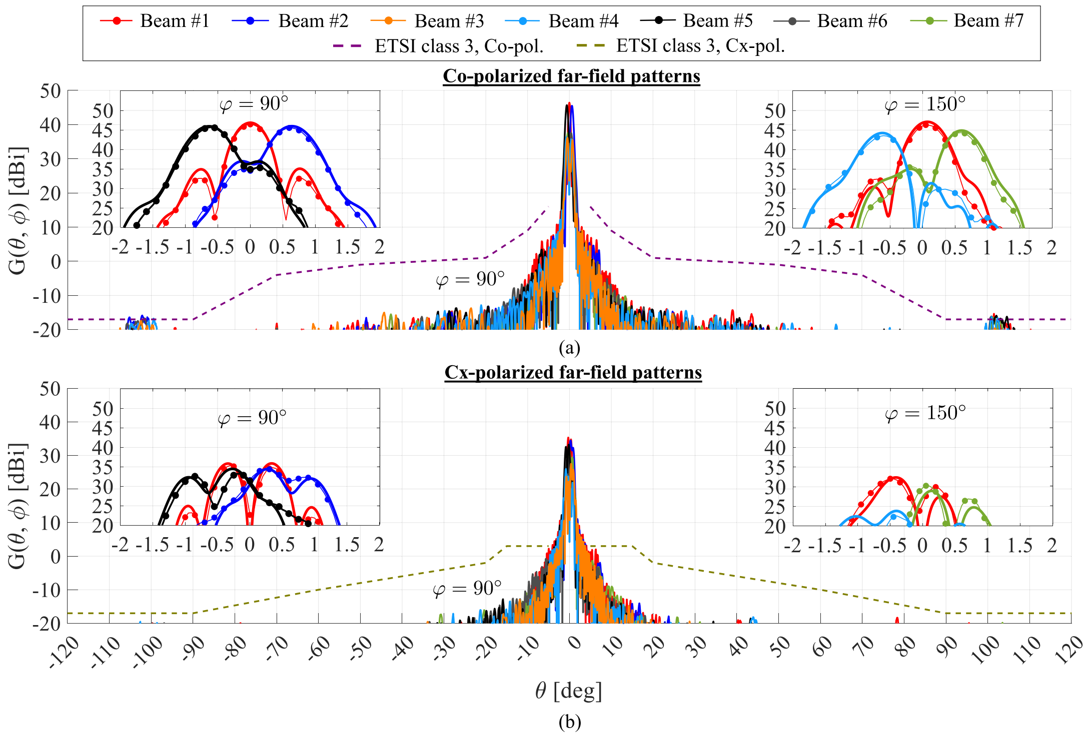

Fig. 13. Passive antenna system G_A for the on-axis beam and two adjacent off-axis beams: measured (symbolic) and simulated (solid) (a) co-polarization and (b) cross-polarization H-plane pattern cuts for the seven synthesized beams; ETSI Class 3 mask for E-band is shown for reference. The low SLL is facilitated by the rim-extended offset parabolic reflector and the pattern shaping of the FPA elements. The beam directions are defined as follows: beam #1 is ($\theta = 0° \quad \forall\varphi$), beam #2 is ($\theta = 0.65°, \varphi = 90°$), beam #3 is ($\theta = 0.65°, \varphi = 30°$), beam #4 is ($\theta = 0.65°, \varphi = 330°$), beam #5 is ($\theta = 0.65°, \varphi = 270°$), beam #6 is ($\theta = 0.65°, \varphi = 210°$), and beam #7 is ($\theta = 0.65°, \varphi = 150°$).

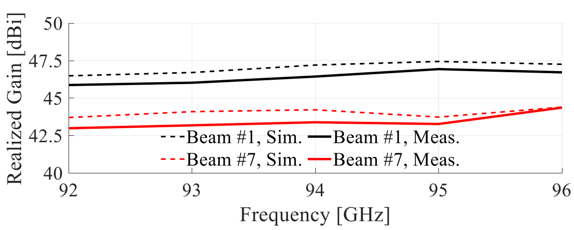

Fig. 14. Simulated and measured G_A for the on-axis and most off-axis beams across frequency, representing the upper and lower bounds.

loads. This preserves the interface reflection conditions while isolating the transmission of each channel.

2) System-EEP Calculation and Interface Mismatch Effects: Because $\Gamma_i \neq 0$, the PA-QOFN interface produces multiple reflections that perturb the port excitations at Ref. 2 and, consequently, the radiated fields. This is accounted for by solving (6) to obtain the interstage waves $\mathbf{a}^p_{\text{ref}}$ at Ref. 2 when pth channel is "ON," and then obtaining the system EEPs, as a superposition, using (7). In practice, when measuring the system EEP associated with channel p, only that channel is switched on, while the others are biased with DPAs "OFF" and HPAs "ON" that preserves Γ_i ($i = 1, \ldots, N$, index across the channels for the fixed p) and blocks the channel transmission. We observe that the shape of $(e_{\text{sys}})_p$ is essentially invariant across AC states q, and state changes primarily scale its complex amplitude. The realized gain and EIRP of the active system are then evaluated directly from (8) and (9). To represent the correct values of the combined realized gain, excluding the PA chain amplification, $|a_{\text{in}}|^2\, \mathbf{c}^{\text{H}}\mathbf{T}^{\text{H}}_{\text{PA}}\mathbf{T}_{\text{PA}}\mathbf{c}$ is used as the total available power at Ref. 2.

3) Excitation for EIRP Analysis: For maximum EIRP, we select $|a_{\text{in}}|^2$, such that each AC operates near its $P_{1\text{dB}}$ limit (phases and magnitudes set by (11), then quantized). Due to the low PA module's transducer gain, a DPA (measured $P_{\text{sat}} = 25.5$ dBm) is used to provide the required input power. Therefore, the DPA compression is presented in the EIRP sweep, but does not affect the synthesis procedure.

4) Limitations of the Beamforming Approach for Practical Systems: In this work, the beamforming is realized using the linearized model, even at a large signal. This approach does not take into account the compression of the PA module, which can vary for the different ACs. In the proposed system, due to the negligible AM–PM conversion, the impact of these effects can be neglected. In this way, the maximization of the $\mathbf{c}_{\text{opt}}$ excitation amplitudes, while maintaining the phases obtained in the small-signal, directly facilitates the maximal EIRP.

B. Beam Patterns and System EIRP

Fig. 15 compares the FPA pEEPs (Ref. 1) with synthesized active system patterns (Ref. 3) for beams #1 and #7 using the cascade of measured $\mathbf{S}_{\text{PA}}$ and $\mathbf{S}_{\text{Ant}}$ and the beamforming approach described in Section VII-A. Discrepancies are small for the beam #1 direction (compared to Fig. 6) and increase for the beam #7 direction due to the increased active reflection coefficient in all QOFN input channels at Ref. 2 (*cf.* wide-angle beamsteering in classical array antennas). Fig. 16 shows the realized gain of the active system for seven beams, based on the measured PA module and passive system. As seen, the G_{sys} values exceed 40 dBi, and the SLLs of the system are similar to those of the passive part. The crossover levels for the selected

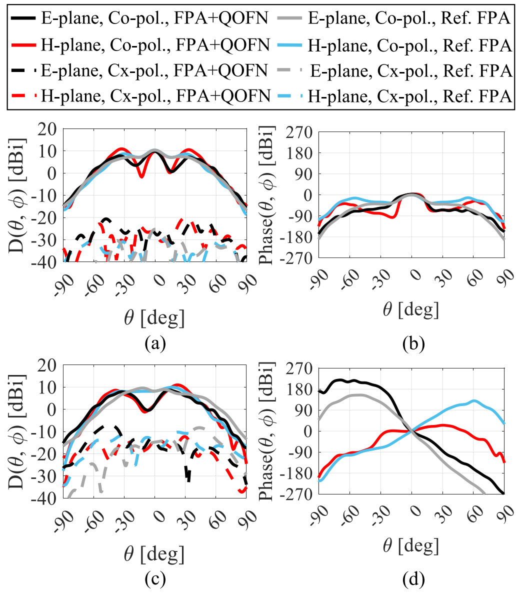

Fig. 15. Measured far-field patterns of the standalone FPA (Ref. 1) versus system far-field patterns with PA module included (Ref. 3), synthesized for two beam directions (a) and (b) on-axis beam #1 and (c) and (d) off-axis beam #7.

TABLE III
SYSTEM EIRP CONTRIBUTIONS AT 94 GHz

Beam	Directivity, dBi	QOFN Loss, dB	PA module $P_{1\mathrm{dB}}$, dBm
Beam #1	50.1	2.3	32
Beam #7	47.7	3.7	31.6

beam directions (which correspond to the sEEP peaks) are approximately −6 dB. The realized gain drop is ≤ 0.5 dB for beam #1 and ≤ 1 dB for the other beams compared to Fig. 13. This demonstrates the relatively low impact of the PA module nonideality. For more continuous beamsteering, we synthesize intermediate beams in the corresponding crossover directions. Fig. 17 shows that the average realized-gain variation is approximately 2 dB and $G_{\mathrm{sys}} > 42$ dBi. Instantaneous field color maps illustrate how the QOFN redistributes the field across the FPA elements while combining input power.

For maximum EIRP, each AC is driven near $P_{1\mathrm{dB}}$ (phases and magnitudes set using (11) and then quantized). The obtained result is compared to the predicted large-signal performance, evaluated using the simulated passive system far-field patterns G_{A}. Fig. 18 shows that at 94 GHz, we achieve 80.6 dBm versus the predicted 81 dBm for beam #1 (the best case) and 75.6 dBm versus the predicted 76.8 dBm for beam #7 (the worst case). Across 92–96 GHz, the EIRP ranges 79.5–80.6 dBm versus the predicted 80–81 dBm (beam #1) and 75.5–76.5 dBm versus the predicted 76.5–77.5 (beam #7). The minimum EIRP across the steered beams is ≥ 75 dBm over the band. Table III includes the EIRP contributions at 94 GHz. As seen, the most significant EIRP change is caused by the directivity degradation of 2.4 dB, where ~1 dB is attributed to the reflector and FPA performance, and ~1.4 dB to the effects of the QOFN. The agreement between simulations and measurements validates the active-system model developed in Section IV.

The stability of the synthesized beam is also evaluated with respect to practical nonidealities. The PA-module state can be reproduced within ±0.3 dB in amplitude and ±2.5° in phase for the transmission coefficient $t_p^{(q)}$ after switching. These variations result in <0.1-dB deviation in peak beam gain and negligible pointing change of <0.1% of the 1° 2-D steering range. This confirms that the beamforming process is robust to realistic amplitude and phase spread between ACs and that steering accuracy is not degraded under the investigated operating conditions.

VIII. DISCUSSION

Table IV compares the proposed W-band active antenna system with the high-EIRP solutions presented in the literature. This work achieves the highest reported EIRP among the compared systems with only $N = 6$ GaAs ACs (PS + DPA + HPA, $P_{1\mathrm{dB}} \approx$ 25–26 dBm each) and an $M = 7$ element FPA. By jointly combining power and steering within the QOFN, the design attains >15–20 dB higher EIRP than large BiCMOS phased arrays at similar bands (e.g., 60 dBm with 256 Tx channels in [10]) while using ~40 times fewer ACs and preserving a compact front end.

Compared to electronically steered reflector/lens antennas at lower millimeter-wave bands, the proposed architecture also achieves higher EIRP. Spherical or torus reflectors with active FPAs at 28–32 GHz reach 60–66-dBm EIRP with tens to hundreds of channels [16], [17], whereas a prime-focus reflector at 71 GHz with an 81-element FPA facilitates ≈70 dBm (simulation) [67]. The D-band elliptical lens antenna [19], fed by an antenna-on-chip feed in 130-nm SiGe BiCMOS technology [23], is not included in our comparison table due to the lack of metrics relevant to high-EIRP solutions. In fact, the work in [19] focuses on scanning (e.g., patterns and directivity) and demonstrates $P_{\mathrm{sat}} = -8$ dBm [23], which is 18 dB smaller than in the present work.

Work [37] shows that EIRP enhancement is achieved through system-level modifications. As mentioned in Section V-B, the FPA excitation for the beams corresponding to the mainlobes of sEEPs (Ref. 1) is dominated by a single FPA element. Maximization of the excitation coefficient amplitudes yields 76–77-dBm EIRP (for the reflector with the FPA); however, the sidelobe level increases. As an alternative, the beam-switching architecture utilized the same number of PAs per beam, can be considered. However, it necessitates the use of a switching network (single-pole-N-throw, SPNT) that has high insertion loss in the W-band (typically ≈ 3 dB per SPDT). This highly impacts the Tx output power and efficiency by introducing significant insertion loss in the system after the final amplification stage. The system, proposed in this work, requires the PSs for its operation, which also have significant insertion loss. However, they are placed before the final amplification stage and do not contribute to the Tx output power and efficiency as significantly as a switching network. The latter is replaced with the proposed QOFN [38] with reduced insertion loss. This allows us to keep the beamforming flexibility and use the contribution from multiple PAs for each generated beam with reduced QOFN loss.

Beam-steering range is the main tradeoff. Silicon-based RFIC phased arrays offer wide-angle coverage (e.g., 30° 2-D in [10]), albeit at much lower EIRP, whereas mechanically steered dual-reflectors provide high gain but add moving parts and actuators and, in some cases, do not satisfy ETSI Class

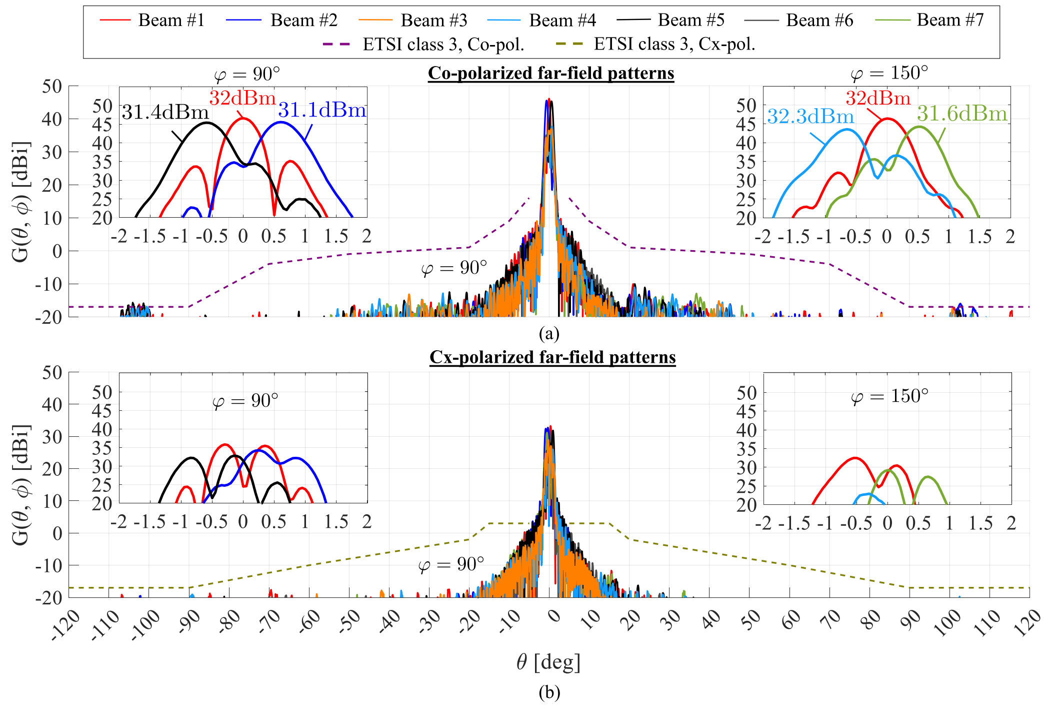

Fig. 16. Active system G_{sys}, based on the measured performance of the PA module at $P_{1\text{dB}}$ and the measured G_{A} of the passive antenna system for the on-axis beam and two adjacent off-axis beams: (a) co-polarization component cuts and (b) cross-polarization cuts; ETSI Class 3 mask shown for reference.

TABLE IV

High EIRP Antenna Solutions Suitable for Millimeter-Wave Frequencies

Ref.	System configuration	Frontend type	P_{sat} per active channel, dBm	# of active channels	# of array elements	Frequency, GHz	Side-lobe mask	Scanning approach	Scanning range	Antenna Peak Realized Gain	Peak EIRP, dBm
[10]	Patch antenna phased array integrated with 0.18-μm SiGe BiCMOS RFIC	Tx/Rx	5	256	256(Tx) / 128(Rx)	95 – 109.5	N/A	Electronic	7HPBW (30°), 2D	$\geq$ 18.5	60
[6]	Gregorian dual-reflector with movable feed	Passive	N/A	N/A	1	71 – 86	Not compliant (ETSI class 3)	Mechanical	±3HPBW (±2.5°)	50	N/A
[67]	Single prime-focus parabolic reflector with FPA	Tx	10‡	81	81	71	N/A	Electronic	1.5HPBW (1°), 2D	$\approx$ 50	70‡
[16]	Spherical reflector with active FPA	Tx	30	49	49	28 – 32	Compliant†	Electronic	4HPBW (8°), 2D	36	66
[17]	Torus reflector with active FPA	Tx/Rx	20	324	324	26 – 30	N/A	Electronic	±15HPBW (±30°), 1D	36	60
[44]	Dielectric lens with feed array	Tx/Rx	> 24	1	64	71 – 76 / 81 – 86	N/A	Electronic	2HPBW (±4°) × 8.5HPBW (±17°), 2D	> 5	34
This work	Single offset parabolic reflector with proposed FPA GaAs frontend	Tx	26	6	7	92 – 96	Compliant (ETSI class 3)	Electronic	2HPBW (1°), 2D	47.7	80

Notes: †The side-lobe mask is not specified, ‡Simulation results only.

3 standard [6]. The present system optimizes for high EIRP within a modest 2HPBW (≈1°) 2-D range. Within this range, all beams comply with ETSI Class 3 except for <1-dB peaks at ±103° caused by the reflector edge diffraction.

Table V provides the link budget examples. The fading margin due to rain, fog, and atmospheric gases (oxygen and water vapor) was considered. As seen, the presented solution can potentially be utilized for millimeter-wave 5-km hops.

Limitations and scalability paths are present. Although the $N < M$ QOFN allows for a lower amount of ACs, it yields an efficiency limitation of QOFN and degraded beamforming flexibility, that is, when beam #7 is generated, leakage to the adjacent FPA elements is presented. Moreover, the insertion loss is QOFN excitation dependent. These drawbacks can be addressed by increasing N ($N > M$) with corresponding geometry optimization. For example, as our simulations predict, while keeping the same $M = 7$, increasing the number of PA channels from 6 to 12 helps to reduce the QOFN insertion loss down to 1.5–2.6 dB from 2.3 to 3.7 dB across frequency. This can also be used for combining the power of relatively low-power Si or SiGe BiCMOS ICs.

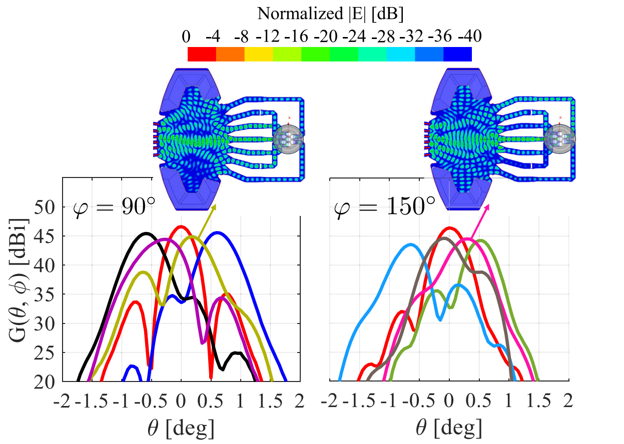

Fig. 17. Beamformed G_{sys} cuts covering the 1° 2-D range at (a) φ = 90° and (b) φ = 150°. Insets: instantaneous E-field in the QOFN structure for the corresponding excitation scenarios.

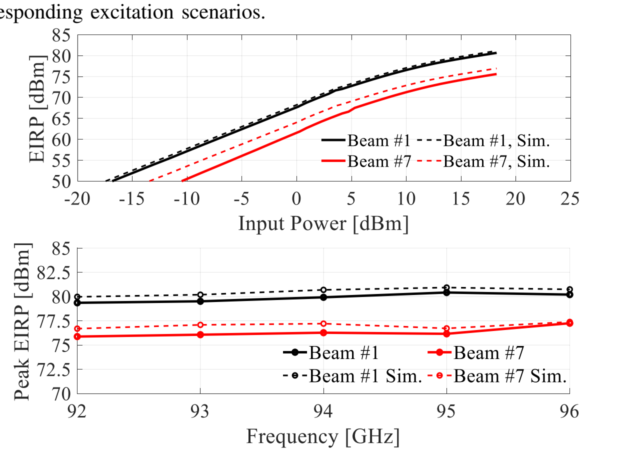

Fig. 18. (Top) EIRP power sweep and (bottom) the peak EIRP over the frequency range for the on-axis beam #1 (the best case) and most off-axis beam #7 (the worst case), based on the measurement (solid) and simulated (dashed) data.

TABLE V

EXAMPLES OF THE LINK BUDGET

Distance, km	1		5	
Path Loss, dB	132		146	
Fading Margin, dB	6.9		26	
Beam Number	#1	#7	#1	#7
P_{Tx}, dBm	32.5	31.5	32.5	31.5
G_{Tx}, G_{Rx}, dBi	48	45	48	45
P_{Rx}, dBm	−10.4	−17.4	−43.5	−50.5

Notes: In practice, an 8 dB back-off is typically considered.

The proposed antenna system scales naturally to a larger beam-steering range. For example, extending the FPA by adding one more ring of elements increases the beam-steering range to ≈ 1.5° (≈2.5 HPBW) (see [62, Figs. 3.9 and 3.10]). This approach preserves the front-end architecture; only the number of QOFN output ports and PA channels grows.

IX. CONCLUSION

We have demonstrated a W-band electronically steerable reflector antenna system that integrates a GaAs TX array with a QOFN to perform joint spatial power combining and beam-steering. The design comprises the 40-cm offset paraboloid with a rim extension and a seven-element FPA of 0.75λ spaced open-ended WG antenna elements. For the presented system, the linearized beamforming approach yielding the closed-form solution for the EIRP maximization was formulated. The integrated active system prototype was fabricated and characterized through measurements. Over steered beams, the minimum EIRP is ≥ 75 dBm, while the on-axis beam level reaches ≈ 80-dBm peak EIRP, with the ETSI Class 3 sidelobe mask compliance except for <1 dB peaks at ±103° caused by the edge diffraction on the reflector rim. The QOFN insertion loss for the present six-input implementation varies within 2.3–3.7 dB depending on the beam and frequency. The active reflection coefficients at the QOFN inputs remain < -8 dB.

Future work will focus on: 1) lower loss and wider-angle operation through QOFN shaping and an increased number of ACs; 2) dual-polarization design implementation; 3) extend the formulation of the beamforming approach to systems with strong nonlinear effects; and 4) perform the modulated-signal testing, including the EVM measurements and evaluation of beam stability. These enhancements extend the presented concept to longer-range 6G backhaul scenarios and multibeam use cases.

REFERENCES

[1] (2021). *Deutsche Telekom, Cosmote and Ericsson Look Beyond 100 GHz to Boost 5G Backhaul Capacity*. [Online]. Available: https://www.ericsson.com/en/news/2021/4/ericsson-trials-w-band-as-5g-backhaul-spectrum

[2] *Microwave Outlook Report 2024*, Ericsson, Stockholm, Sweden, 2024.

[3] *Lessons Learned From a Decade With E-Band*, Ericsson, Stockholm, Sweden, 2019.

[4] L. Manholm, S. Agneessens, P. Lauri, and C. Fougstedt, "Field trial with a 50 dBi E-band sway compensating reflector antenna," in *Proc. 19th Eur. Conf. Antennas Propag. (EuCAP)*, Mar. 2025, pp. 1–5.

[5] O. Talcoth and L. Manholm, "A steerable 50 dBi E-band reflector antenna using a contactless waveguide joint," in *Proc. 19th Eur. Conf. Antennas Propag. (EuCAP)*, Mar. 2025, pp. 1–5.

[6] E. Wang et al., "A 50 dBi E-band dual-reflector antenna for 5G backhauling with auto-beam-tracking function," *IEEE Trans. Antennas Propag.*, vol. 72, no. 6, pp. 4874–4887, Jun. 2024.

[7] (2023). *Sway Compensation Antennas, Your E-Band Friend, With Benefits*. [Online]. Available: https://www.ericsson.com/en/blog/2023/3/sway-compensation-antennas

[8] S. Shahramian, M. J. Holyoak, and Y. Baeyens, "A 16-element W-band phased-array transceiver chipset with flip-chip PCB integrated antennas for multi-gigabit wireless data links," *IEEE Trans. Microw. Theory Techn.*, vol. 66, no. 7, pp. 3389–3402, 2018.

[9] A. Natarajan, A. Valdes-Garcia, B. Sadhu, S. K. Reynolds, and B. D. Parker, "W-band dual-polarization phased-array transceiver front-end in SiGe BiCMOS," *IEEE Trans. Microw. Theory Techn.*, vol. 63, no. 6, pp. 1989–2002, May 2015.

[10] S. Shahramian, M. J. Holyoak, A. Singh, and Y. Baeyens, "A fully integrated 384-element, 16-tile, *W*-band phased array with self-alignment and self-test," *IEEE J. Solid-State Circuits*, vol. 54, no. 9, pp. 2419–2434, Sep. 2019.

[11] D. Zhao, P. Yu, S. Jiang, W. Gao, P. He, and H. Liu, "W-band CMOS beamforming ICs and integrated phased-array antennas with 20+ Gb/s data rates," *Sci. China Inf. Sci.*, vol. 67, no. 11, Nov. 2024, Art. no. 212301.

[12] W. Shin, B.-H. Ku, O. Inac, Y.-C. Ou, and G. M. Rebeiz, "A 108–114 GHz 4×4 wafer-scale phased array transmitter with high-efficiency on-chip antennas," *IEEE J. Solid-State Circuits*, vol. 48, no. 9, pp. 2041–2055, 2013.

[13] A. Dubok et al., "Double-reflector configuration for optimal exposure of wideband focal-plane arrays with optical beamforming," *IEEE Trans. Antennas Propag.*, vol. 65, no. 8, pp. 4316–4321, Aug. 2017.

[14] H. Chreim et al., "An enhanced Ka-band reflector focal-plane array using a multifeed EBG structure," *IEEE Antennas Wireless Propag. Lett.*, vol. 9, pp. 1152–1156, 2010.

[15] A.-E. Mahmoud, W. Hong, Y. Zhang, and A. Kishk, "W-band mutlilayer perforated dielectric substrate lens," *IEEE Antennas Wireless Propag. Lett.*, vol. 13, pp. 734–737, 2014.

[16] B. Rohrdantz, T. Jaschke, T. Reuschel, S. Radzijewski, A. Sieganschin, and A. F. Jacob, "An electronically scannable reflector antenna using a planar active array feed at Ka-band," *IEEE Trans. Microw. Theory Techn.*, vol. 65, no. 5, pp. 1650–1661, May 2017.

[17] A. Elsakka et al., "A mm-wave phased-array fed torus reflector antenna with $\pm 30^{\circ}$ scan range for massive-MIMO base-station applications," *IEEE Trans. Antennas Propag.*, vol. 70, no. 5, pp. 3398–3410, May 2022.

[18] N. R. Erickson, G. Narayanan, J. C. Bardin, K. F. Warnick, B. D. Jeffs, and J. Diao, "A 64 element, 70–95 GHz focal plane phased array," in *Proc. IEEE Int. Symp. Antennas Propag. USNC/URSI Nat. Radio Sci. Meeting*, Jul. 2015, pp. 1514–1515.

[19] M. Arias Campo et al., "D-band demonstration of quasi-optical and analog beam reconfiguration using phased array and lens for 6G applications," *IEEE Trans. Antennas Propag.*, vol. 73, no. 8, pp. 5064–5074, Aug. 2025.

[20] H. Wang et al. (2023). [Online]. Available: https://ideas.ethz.ch/research/surveys/pa-survey.html

[21] P. Song, A. C. Ulusoy, R. L. Schmid, S. N. Zeinolabedinzadeh, and J. D. Cressler, "W-band SiGe power amplifiers," in *Proc. IEEE Bipolar/BiCMOS Circuits Technol. Meeting (BCTM)*, Sep. 2014, pp. 151–154.

[22] C. R. Chappidi and K. Sengupta, "A W-band SiGe power amplifier with P_{sat} of 23 dbm and PAE of 16.8% at 95 GHz," in *IEEE MTT-S Int. Microw. Symp. Dig.*, Jun. 2017, pp. 1699–1702.

[23] A. Karakuzulu, W. A. Ahmad, D. Kissinger, and A. Malignaggi, "A four-channel bidirectional D-band phased-array transceiver for 200 Gb/s 6G wireless communications in a 130-nm BiCMOS technology," *IEEE J. Solid-State Circuits*, vol. 58, no. 5, pp. 1310–1322, May 2023.

[24] M. Micovic et al., "92–96 GHz GaN power amplifiers," in *IEEE MTT-S Int. Microw. Symp. Dig.*, Jun. 2012, pp. 1–3.

[25] P. Huang et al., "A 94 GHz monolithic high output power amplifier," in *IEEE MTT-S Int. Microw. Symp. Dig.*, vol. 3, Jun. 1997, pp. 1175–1178.

[26] (2021). *GAPZ0095A W-Band Power Amplifier 92–96 GHz (85-100 GHz)*. Accessed: Oct. 14, 2024. [Online]. Available: https://gotmic.se

[27] K. Ma, S. Mou, Y. Lu, L. K. Meng, and K. S. Yeo, "A 60GHz defected ground power divider using SiGe BiCMOS technology," in *Proc. Int. SoC Design Conf.*, Nov. 2011, pp. 1–4.

[28] M. Pittermann, T. Zwick, and A. Bhutani, "A 53–125 GHz chip to double-ridge rectangular waveguide transition," *Electron. Lett.*, vol. 60, no. 6, p. 13153, Mar. 2024.

[29] H. Cheng, X. Zhu, F. Hou, W. Wang, L. Shen, and S. Hu, "Compact 31-W 96-GHz amplifier module in GaN-MEMS for wireless communications," *IEEE Trans. Microw. Theory Techn.*, vol. 70, no. 2, pp. 1233–1241, Feb. 2022.

[30] C. Yi, H. Lee, K. J. Lee, J. H. Joo, J. B. Kwon, and M. Kim, "Uniform-field over-mode waveguide for spatial power-combining applications," *IEEE Microw. Wireless Compon. Lett.*, vol. 28, no. 1, pp. 10–12, Jan. 2018.

[31] P. Kaul, A. Aljarosha, A. B. Smolders, M. K. Matters-Kammerer, and R. Maaskant, "Waveguide integration and packaging of a multi-channel power amplifier in a SiGe BiCMOS technology for mm-wave applications," *IEEE Trans. Compon., Packag., Manuf. Technol.*, vol. 14, no. 11, pp. 2020–2031, Nov. 2024.

[32] S. Bahrami, D. Lee, W. Hong, and H.-J. Song, "Excitation flexibility of on-antenna power combining," *IEEE Antennas Wireless Propag. Lett.*, vol. 22, pp. 1376–1380, 2023.

[33] N.-S. Cheng, A. Alexanian, M. G. Case, D. B. Rensch, and R. A. York, "40-W CW broad-band spatial power combiner using dense finline arrays," *IEEE Trans. Microw. Theory Techn.*, vol. 47, no. 7, pp. 1070–1076, Jul. 1999.

[34] A. Roev, J. Qureshi, M. Geurts, R. Maaskant, M. K. Matters-Kammerer, and M. Ivashina, "A wideband mm-wave watt-level spatial power-combined power amplifier with 26% PAE in SiGe BiCMOS technology," *IEEE Trans. Microw. Theory Techn.*, vol. 70, no. 10, pp. 4436–4448, Oct. 2022.

[35] S. Li, T. Chi, and H. Wang, "Multi-feed antenna and electronics co-design: An E-band antenna-LNA front end with on-antenna noise-canceling and G_m-boosting," *IEEE J. Solid-State Circuits*, vol. 55, no. 12, pp. 3362–3375, Dec. 2020.

[36] O. A. Iupikov et al., "A cavity-backed patch antenna with distributed multi-port feeding, enabling efficient integration with Doherty power amplifier and band-pass filter," *IEEE Trans. Antennas Propag.*, vol. 69, no. 8, pp. 4412–4422, Aug. 2021.

[37] V. Chernikov, A. Vilenskiy, and M. Ivashina, "Analysis of millimeter-wave array frontend architectures for high EIRP: Comparing various beamforming and power combining techniques," in *Proc. 19th Eur. Conf. Antennas Propag. (EuCAP)*, Mar. 2025, pp. 1–5.

[38] A. R. Vilenskiy, S. Y. Chaudhry, H.-T. Chou, and M. V. Ivashina, "Millimeter-wave array antenna architectures employing joint power combining and beam steering for next-generation backhaul applications," in *Proc. 17th Eur. Conf. Antennas Propag. (EuCAP)*, Mar. 2023, pp. 1–5.

[39] Y. J. Guo, M. Ansari, R. W. Ziolkowski, and N. J. G. Fonseca, "Quasi-optical multi-beam antenna technologies for B5G and 6G mmWave and THz networks: A review," *IEEE Open J. Antennas Propag.*, vol. 2, pp. 807–830, 2021.

[40] D. Wang, K.-D. Xu, Y. Cao, C. Guo, and S. Yan, "A Butler matrix-based multibeam W-band slot antenna array fabricated by metal additive manufacturing technology," *IEEE Trans. Antennas Propag.*, vol. 72, no. 6, pp. 5349–5354, Jun. 2024.

[41] J. S. Park, T. Chi, and H. Wang, "An ultra-broadband compact mm-wave Butler matrix in CMOS for array-based MIMO systems," in *Proc. IEEE Custom Integr. Circuits Conf.*, Sep. 2013, pp. 1–4.

[42] D. Nüßler and H.-H. Fuchs, "A Rotman lens at W-band," *Frequenz*, vol. 56, nos. 11–12, pp. 244–248, Nov. 2002.

[43] Y. Gao, M. Khaliel, F. Zheng, and T. Kaiser, "Rotman lens based hybrid analog–digital beamforming in massive MIMO systems: Array architectures, beam selection algorithms and experiments," *IEEE Trans. Veh. Technol.*, vol. 66, no. 10, pp. 9134–9148, Oct. 2017.

[44] J. Ala-Laurinaho et al., "2-D beam-steerable integrated lens antenna system for 5G E-band access and backhaul," *IEEE Trans. Microw. Theory Techn.*, vol. 64, no. 7, pp. 2244–2255, Jun. 2016.

[45] M. V. Ivashina, O. Iupikov, R. Maaskant, W. A. van Cappellen, and T. Oosterloo, "An optimal beamforming strategy for wide-field surveys with phased-array-fed reflector antennas," *IEEE Trans. Antennas Propag.*, vol. 59, no. 6, pp. 1864–1875, Jun. 2011.

[46] A. Salmi, A. Lehtovuori, and V. Viikari, "On realized gain-optimal feeding coefficients of antenna arrays," in *Proc. 17th Eur. Conf. Antennas Propag. (EuCAP)*, Mar. 2023, pp. 1–5.

[47] S. Stein, "On cross coupling in multiple-beam antennas," *IRE Trans. Antennas Propag.*, vol. 10, no. 5, pp. 548–557, Sep. 1962.

[48] V. S. Chernikov, A. R. Vilenskiy, S. Agneessens, L. Manholm, and M. V. Ivashina, "A W-band choke-ring encircled focal plane array of full-metal elements for reflector antennas with over 50%-efficiency high crossover beams," *IEEE Antennas Wireless Propag. Lett.*, vol. 23, pp. 4578–4582, 2024.

[49] K. F. Warnick, D. B. Davidson, and D. Buck, "Embedded element pattern loading condition transformations for phased array modeling," *IEEE Trans. Antennas Propag.*, vol. 69, no. 3, pp. 1769–1774, Mar. 2021.

[50] K. F. Warnick and B. D. Jeffs, "Gain and aperture efficiency for a reflector antenna with an array feed," *IEEE Antennas Wireless Propag. Lett.*, vol. 5, pp. 499–502, 2006.

[51] A. K. Bhattacharyya, *Phased Array Antennas: Floquet Analysis, Synthesis, BFNs and Active Array Systems*. Hoboken, NJ, USA: Wiley, 2006.

[52] C. A. Balanis, *Antenna Theory: Analysis and Design*. Hoboken, NJ, USA: Wiley, 2016.

[53] E. G. Geterud, J. Yang, T. Ostling, and P. Bergmark, "Design and optimization of a compact wideband hat-fed reflector antenna for satellite communications," *IEEE Trans. Antennas Propag.*, vol. 61, no. 1, pp. 125–133, Jan. 2013.

[54] V. S. Chernikov, A. R. Vilenskiy, and M. V. Ivashina, "Design considerations for focal-plane array antennas for 6G millimeter-wave backhaul links," in *Proc. IEEE Int. Symp. Antennas Propag. USNC-URSI Radio Sci. Meeting (USNC-URSI)*, Jul. 2023, pp. 765–766.

[55] T. A. Milligan, *Modern Antenna Design*. Hoboken, NJ, USA: Wiley, 2005.

[56] J. Cao, W. Wang, W. Song, and B. Chen, "Study of the scanning characteristics of on-board reflector antenna with 7-feed cluster," *J. Phys., Conf. Ser.*, vol. 1802, no. 2, Mar. 2021, Art. no. 022090.

[57] P.-S. Kildal, *Foundations of Antenna Engineering: A Unified Approach for Line-of-Sight and Multipath*. Norwood, MA, USA: Artech House, 2015.

[58] A. Cornejo, S. Landeros-Ayala, R. Martinez-Rodriguez, and J. M. Matías, "Interference evaluations in frequency reuse by using offset-parabolic-reflector antennas for a uhts system," *Int. J. Eng. Sci.*, vol. 7, no. 8, pp. 34–45, 2018.

[59] I. P. Theron, R. Lehmensiek, and D. I. L. de Villiers, "The design of the MeerKAT dish optics," in *Proc. Int. Conf. Electromagn. Adv. Appl.*, Sep. 2012, pp. 539–542.

[60] I. P. Theron, R. Lehmensiek, and D. I. L. de Villiers, "Towards an optics design for the SKA," in *Proc. Africon*, Sep. 2013, pp. 1–5.

[61] D. I. L. de Villiers and R. Lehmensiek, "Sub-reflector extensions for reduced noise temperature in low-side sub-reflector offset Gregorian systems," in *Proc. 6th Eur. Conf. Antennas Propag. (EUCAP)*, Mar. 2012, pp. 3438–3441.

[62] V. Chernikov. *Focal Plane Arrays for Millimeter-Wave Beam-Steering Wireless Backhaul Antenna Systems*. Accessed: Sep. 26, 2025. [Online]. Available: https://research.chalmers.se/publication/548119

[63] A. R. Vilenskiy, Y. Zhang, and M. V. Ivashina, "Methods for attenuating and terminating waves in ridge gap waveguide at W-band: Carbon-loaded foam, carbonyl iron paint, and nickel plating," in *Proc. 51st Eur. Microw. Conf. (EuMC)*, Apr. 2022, pp. 217–220.

[64] V. Vassilev, A. Vilenskiy, H.-T. Chou, M. Ivashina, and H. Zirath, "A 55–105 GHz PIN diode SPDT switch," in *Proc. Int. Symp. Antennas Propag. (ISAP)*, Oct. 2021, pp. 1–2.

[65] (2021). *GPSH0012A W-Band 5-Bit Phase Shifter 92–96 GHz*. Accessed: Jan. 20, 2026. [Online]. Available: https://gotmic.se

[66] (2021). *GAPZ0100A W-Band Medium Power Amplifier 92-100 GHz (88-104 GHz)*. Accessed: Jan. 20, 2026. [Online]. Available: https://gotmic.se

[67] A. Al-Rawi, A. Dubok, S. J. Geluk, B. P. de Hon, M. H. A. J. Herben, and A. B. Smolders, "Increasing the EIRP by using FPA-fed reflector antennas," in *Proc. IEEE Int. Symp. Antennas Propag. (APSURSI)*, Jun. 2016, pp. 1623–1624.

Viktor S. Chernikov (Graduate Student Member, IEEE) received the B.Sc. and M.Sc. degrees (summa cum laude) in radioengineering and telecommunication from Saint-Petersburg State Electrotechnical University "LETI," Saint-Petersburg, Russia, in 2020 and 2022, respectively, and the Licentiate of Engineering degree from the Chalmers University of Technology, Gothenburg, Sweden, in 2025, where he is currently pursuing the Ph.D. degree with the Antenna Systems Group.

From 2020 to 2022, he worked as an RF Electronics Engineer at the Institute of Applied Astronomy, Russian Academy of Science (RAS), Saint-Petersburg. His research interests include applied electromagnetics, antenna and front-end architectures, and integrated circuit design.

Artem R. Vilenskiy (Senior Member, IEEE) received the Specialist degree (summa cum laude) in radioengineering and the Ph.D. degree in antennas and microwave devices from Bauman Moscow State Technical University, Moscow, Russia, in 2011 and 2014, respectively.

From 2011 to 2019, he was with the Samsung Research Institute, Moscow, where he had roles of a Researcher, an Expert Engineer, and the Project Leader at the Electromagnetics Group and RF Sensor Part. From 2015 to 2019, he was a Visiting Associate Professor at the Radio-Electronic Systems and Devices Department, Bauman Moscow State Technical University. From 2019 to 2024, he was a Researcher with the Antenna Systems Group, Chalmers University of Technology, Gothenburg, Sweden. He is currently a Microwave Team Lead at XPANCEO, Dubai, United Arab Emirates. His research interests include applied and computational electromagnetics, antenna and front-end IC design, and controllable high-frequency materials and devices.

Göran Granström received the M.Sc. degree in electrical engineering from the Chalmers University of Technology, Gothenburg, Sweden, in 2010.

He spent the following three years as a Microwave Design Consultant at RUAG Space, Gothenburg. In 2013, he joined Gotmic AB, Gothenburg, to develop high-performance mm-wave circuits, and since 2025, as the Head of product development. His research interests include MMIC circuits, power amplifiers, transmitters, and receivers.

Lars Manholm received the M.Sc. degree in electrical engineering and the Licentiate of Technology degree in electromagnetics from the Chalmers University of Technology, Gothenburg, Sweden, in 1994 and 1998, respectively.

He joined Ericsson Microwave Systems, Gothenburg, as an Antenna Designer, in 1998, and Ericsson Research, Gothenburg, in 2003, where he holds a position as a Master Researcher in antenna hardware. His research interests include electronically steerable antennas and antenna arrays for cellular base stations and fixed radio link applications at microwave and millimeter-wave frequencies.

Sam Agneessens (Member, IEEE) received the M.S. and Ph.D. degrees in electrical engineering from Ghent University, Ghent, Belgium, in 2011 and 2015, respectively.

He was a Post-Doctoral Fellow of Research Foundation-Flanders (FWO-V) affiliated with Ghent University and imec, Leuven, Belgium, and became an Assistant Professor at Ghent University in 2017. He joined Ericsson AB, Gothenburg, Sweden, in 2018, as a Senior Researcher. He currently leads the wireless transport research project at Ericsson. His research background is in electromagnetics, focusing on robust antenna systems for wearable applications and mmWave systems.

Dr. Agneessens received the URSI Young Scientist Award from the 2014 URSI General Assembly and was awarded the 2014 Premium Award for Best Paper in *IET Electronics Letters*.

Marcus Gavell (Member, IEEE) was born in Eskilstuna, Sweden, in 1981. He received the M.Sc. and Ph.D. degrees in electrical engineering from the Chalmers University of Technology, Gothenburg, Sweden, in 2005 and 2018, respectively.

In 2008, he joined Gotmic AB, Gothenburg, after working as a Radio Verification Engineer with Ericsson AB, Gothenburg. Since 2015, he has been the CTO with Gotmic AB. His current research interests include millimeter-wave MMIC design, in particular, transmitters, receivers, power amplifiers, and predistortion circuits.

Marianna V. Ivashina (Senior Member, IEEE) received the Ph.D. degree in electrical engineering from Sevastopol National Technical University (SNTU), Sevastopol, Ukraine, in 2001.

From 2001 to 2010, she was with the Netherlands Institute for Radio Astronomy (ASTRON), Dwingeloo, The Netherlands, and from 2002 to 2003, she also stayed as a Visiting Scientist with the European Space Agency, ESTEC, Noordwijk, The Netherlands. In January 2011, she published extensively on the above topics, having authored/co-authored over 130 journal and conference papers. She joined the Chalmers University of Technology, Gothenburg, Sweden, where she is currently a Full Professor and the Head of the Antenna Systems Group, Department of Electrical Engineering. Her current research interests include antenna array systems and integration of antennas with active electronic components.

Prof. Ivashina was previously an Associate Editor of IEEE TRANSACTIONS ON ANTENNAS AND PROPAGATION and is currently a Board Member of European School of Antennas (ESoA). Since 2021, she has been the Delegate of the European Association of Antennas and Propagation (EurAAP) for Region 6: Iceland, Norway, and Sweden.